JGR Planets

RESEARCH ARTICLE
10.1029/2023JE007836

Multidisciplinary Analysis of the Nippur Sulcus Region on Ganymede

Federico Tosi[1], Valentina Galluzzi[1], Alice Lucchetti[2], Roberto Orosei[3], Gianrico Filacchione[1], Francesca Zambon[1], Gabriele Cremonese[2], Pasquale Palumbo[1], and Giuseppe Piccioni[1]

[1]INAF-IAPS, Roma, Italy, [2]INAF-OAPd, Padova, Italy, [3]INAF-IRA, Bologna, Italy

Key Points:

- We focus on the Nippur Sulcus region on Ganymede to perform a detailed geological and compositional analysis of this region
- Nippur's grooves have a composition similar to that of small fresh craters and may penetrate 125–135 km into the icy crust
- To reveal potential links between the surface and subsurface liquid pockets, clutter-induced noise must be treated adequately in radar data

Correspondence to:
F. Tosi,
federico.tosi@inaf.it

Citation:
Tosi, F., Galluzzi, V., Lucchetti, A., Orosei, R., Filacchione, G., Zambon, F., et al. (2023). Multidisciplinary analysis of the Nippur Sulcus region on Ganymede. *Journal of Geophysical Research: Planets*, *128*, e2023JE007836. https://doi.org/10.1029/2023JE007836

Received 22 MAR 2023
Accepted 11 JUL 2023
Corrected 4 AUG 2023 and 31 JUL 2024

This article was corrected on 4 AUG 2023 and 31 JUL 2024. See the end of the full text for details.

Author Contributions:
Conceptualization: Federico Tosi
Formal analysis: Valentina Galluzzi, Alice Lucchetti, Roberto Orosei, Gianrico Filacchione, Francesca Zambon
Funding acquisition: Federico Tosi
Investigation: Valentina Galluzzi, Alice Lucchetti, Roberto Orosei, Gianrico Filacchione, Francesca Zambon
Methodology: Federico Tosi, Valentina Galluzzi, Alice Lucchetti, Roberto Orosei, Gianrico Filacchione, Francesca Zambon
Project Administration: Federico Tosi
Software: Roberto Orosei
Supervision: Federico Tosi

Abstract On Jupiter's largest moon Ganymede, we focus on the southern region of Nippur Sulcus, including the Epigeus palimpsest crater. This region displays geologically recent terrains and has good coverage of optical and near infrared remote sensing data, primarily returned by the NASA Galileo mission. We first use high-resolution optical imagery to carry out a detailed geological mapping. We combine hyperspectral data to infer the surface composition of this area. We then apply two theoretical models. The first is a self-similar clustering that uses the mapping of the grooves present in this region to infer the thickness of the ice shell. A second model is used to estimate the radar clutter noise induced by the estimated local topography, which is key for constraining future radar measurements. Based on all findings, we provide a possible evolutionary history of the Nippur Sulcus and Epigeus areas. This exercise shows the potential of an interdisciplinary data analysis combining wide-ranging scientific objectives such as geology, surface composition, and geophysics in view of the future close exploration that will be conducted on Ganymede by the JUICE spacecraft. Our work combines multiple analysis techniques that could be applied to other regions of interest and will prove crucial when JUICE data become available.

Plain Language Summary On Jupiter's largest moon Ganymede, we focus on the region of Nippur Sulcus, including the Epigeus palimpsest crater covered by optical and near infrared remote sensing data acquired in the past by the NASA Galileo mission, to carry out a detailed geological and compositional analysis of this region. We then apply two theoretical models focusing on the estimation of the grooves' depth and on the radar clutter noise induced by the local topography to show how an in-depth analysis combining geology, surface composition, and geophysics could achieve a broader understanding of a given region of interest. For high-priority regions of interest to be studied by JUICE in detail, such a multidisciplinary analysis could ultimately reveal connections between the surface and fluid subsurface.

1. Introduction

We present a study aimed at emphasizing the combination of data returned by multiple remote sensing instruments. The study we conduct here uses both the best data currently available for Ganymede, that is, those returned by the NASA Galileo mission (Johnson et al., 1992) that operated in the Jupiter system in the period 1995–2003, and simulations of the interior of the satellite, which are still unexplored. We focus on the Nippur Sulcus region of Ganymede for the following four reasons: (a) it was well covered by optical and near infrared remote sensing data from the Galileo mission, (b) it displays different terrain categories, including those representative of geologically recent areas, (c) it is located at low-to-moderate latitudes and as such it should be quite shielded by the intrinsic magnetic field of Ganymede against exogenous effects on the observed composition, and (d) it is located in the anti-Jovian hemisphere, which is optimal for future direct observation by ice penetrating radars.

In Section 2, we discuss the geologic context of the Nippur Sulcus region based on past geological mapping and show the current coverage of optical and infrared remote sensing data returned by the Galileo mission. In Section 3, we discuss the surface composition of the Nippur region as inferred by infrared reflectance spectroscopy. In this regard, the resolution of spectroscopic data acquired by the Galileo mission can highlight the abundance of water ice versus non-ice material and characterize the grain size of water ice, although it is insufficient to unambiguously discriminate non-ice compounds and organic compounds, a goal which is left to future exploration. In Section 4, we model the Nippur region from a geophysical point of view, using a relationship that links the length and depth of the extensional faults ("*grooves*"), which are typical features on Ganymede, with

Validation: Federico Tosi
Writing – original draft: Federico Tosi, Valentina Galluzzi, Alice Lucchetti, Roberto Orosei, Gianrico Filacchione, Francesca Zambon
Writing – review & editing: Gabriele Cremonese, Pasquale Palumbo, Giuseppe Piccioni

the aim of quantitatively estimating the thickness of brittle ice in the outer crust and the depth at which the ocean might be found. In Section 5, we focus on modeling the distortion ("*clutter*") in the signal measured by an ice penetrating radar like Radar for Icy Moon Exploration (RIME) onboard JUICE. To this end, since there are no topographic models derived from stereo pairs in the Nippur Sulcus region, we first create a synthetic topographic model starting from the available high-resolution optical imagery and then we simulate the defraction of radar waves due to the rough surface, a technique which was already successfully tested on Mars. Finally, in Section 6 we comment on the results as a whole and in Section 7 we discuss the potential implications of a joint analysis of the remote sensing data that the ESA JUICE mission may obtain in the future on specific regions of interest of Ganymede such as this one.

2. Geological Setting

2.1. ROI Description

The Region Of Interest (ROI) between 167.4°–193.5°E and 16.8°–38.2°N (Figure 1) is dominated by the southern part of NNW-SSE trending Nippur Sulcus that separates the Galileo Regio to the east from the northern part of Marius Regio. The southern central area of the ROI is characterized by the 350-km-wide Epigeus palimpsest crater that marks the transition between Nippur Sulcus and the northern 500-km-wide part of Uruk Sulcus to the south. Uruk Sulcus further branches to the west with the 150-km-wide NW-SE trending Mashu sulcus, which in turn separates the northwestern dark terrain area from Marius Regio to the southwest.

Previous studies propose geological analyses of the area based either on Voyager imagery (Figure 2a, Guest et al., 1988; Murchie & Head, 1989; Underwood et al., 1997) or Voyager/Galileo imagery (Figure 2b, Collins et al., 2013; Patterson et al., 2010). The Voyager-based geological mapping campaign consists of a 1:5,000,000-scale quadrangle geological map series. The ROI here analyzed is located at the boundary of three different quadrangles: (a) the Uruk Sulcus quadrangle (Jg-8, Guest et al., 1988); (b) the Philus Sulcus quadrangle (Jg-4, Murchie & Head, 1989); and (c) the Galileo Regio quadrangle (Jg-3, Underwood et al., 1997). These maps offer high mapping detail of craters with diameters as small as 10 km and, although released in a time span of almost 10 years, show a good match of contacts and units between the quadrangle boundaries (Figure 2a). Conversely, the Voyager/Galileo-based global geological map of Ganymede (Collins et al., 2013; Patterson et al., 2010) offers a uniform 1:15,000,000-scale regional view of the area and high facies detail within the sulci, although less detail is present for other features such as craters (Figure 2b).

These maps show that the Epigeus crater palimpsest overlaps and mantles the surrounding terrains (see also Jones et al. (2003)), thus being the youngest feature of its size in this area that will be hereafter referred to as the "Epigeus ROI."

To fully characterize the Epigeus ROI, we conduct a new geological investigation of the area that considers the previous geological maps and unifies the geological interpretation from separate works (Collins et al., 2013; Guest et al., 1988; Jones et al., 2003; Murchie & Head, 1989; Patterson et al., 2010; Underwood et al., 1997).

2.2. Data and Methods

We use the controlled global Ganymede mosaic at 359 m/pixel from Voyager and Galileo images as the main reference basemap (Kersten et al., 2021) and higher resolution Galileo Solid-State Imaging (SSI) frames (Belton et al., 1992). SSI frames were processed with the planetary image processing *Integrated Software for Imagers and Spectrometers* v3 (ISIS3) of the United States Geological Survey (USGS). These map-projected frames were then further georeferenced manually with the ArcMap software to precisely match the reference basemap (which is slightly offset with respect to the previous basemaps) at the pixel scale (Figure 1). The image frames have a spatial resolution of 90 m/pixel (*5481r–5521r*), 189 m/pixel (*2400r*), and 935 m/pixel (*7800r*). The lowest resolution frame has been included because it offers slightly different illumination conditions that favor the morphological interpretation of the terrains (i.e., SSI frame *7800r* has higher solar incidence angles with respect to the basemap).

We follow the USGS planetary mapping guidelines (Skinner et al., 2018) and use the Federal Geographic Data Committee recommended symbology for planetary geologic maps. The linework is done at a mapping scale of about 1:1,000,000 to be consistent with a readable output scale at 1:5,000,000, which is comparable with the Voyager geological maps that hitherto offer the highest map-scale available (Guest et al., 1988; Murchie & Head, 1989; Underwood et al., 1997).

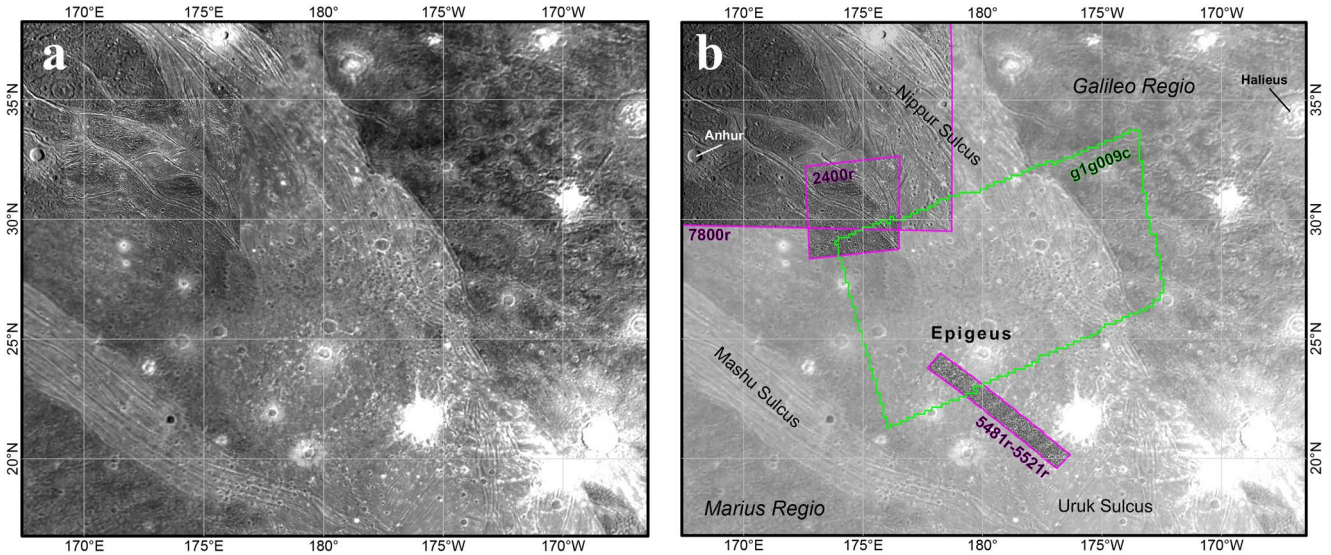

Figure 1. (a) Controlled global Ganymede mosaic (Kersten et al., 2021) showing the Epigeus Region Of Interest (ROI) location and (b) overview of Epigeus ROI main features and available data set (basemap in panel (a)) is shown with 50% transparency. The colored outlines indicate the location of available Solid-State Imaging footprints (magenta) and Near Infrared Mapping Spectrometer footprint (green).

In our geological investigation, we adopt a pure morpho-stratigraphic method by identifying geological units based on their brightness/color and texture (what is sharper and brighter is generally younger than what is darker and has no sharp edges). Following this approach, we classify crater materials into three degradation classes (*c1* to *c3*, from most degraded to freshest craters), consistent with all previous studies. Crater palimpsest units were treated separately to enhance their stratigraphic position with respect to other crater materials, which is consistent with previous studies. We adopt three kinds of geological contacts (certain, approximate, and concealed) and several linear features describing the apparent morphological features. Troughs and ridges within the sulci were only drawn where these are more prominent, avoiding cluttering the figure by drawing every single groove visible in the basemaps. A more detailed structural mapping of Nippur Sulcus grooves is treated separately in Section 4.

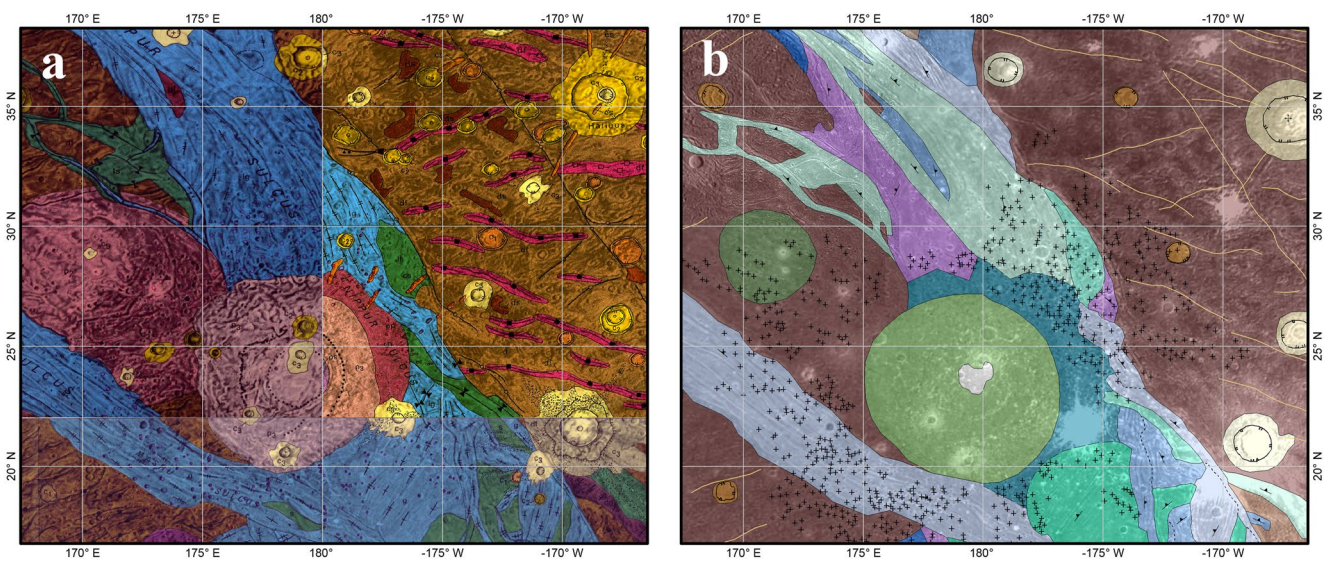

Figure 2. Geological maps of the Epigeus Region Of Interest: (a) Reprojected quadrangles of the Voyager-based geological mapping campaign of Jg-4 (left, Murchie & Head, 1989), Jg-3 (right, Underwood et al., 1997), and Jg-8 (bottom, Guest et al., 1988); (b) Voyager/Galileo-based global geological map of Ganymede (Collins et al., 2013).

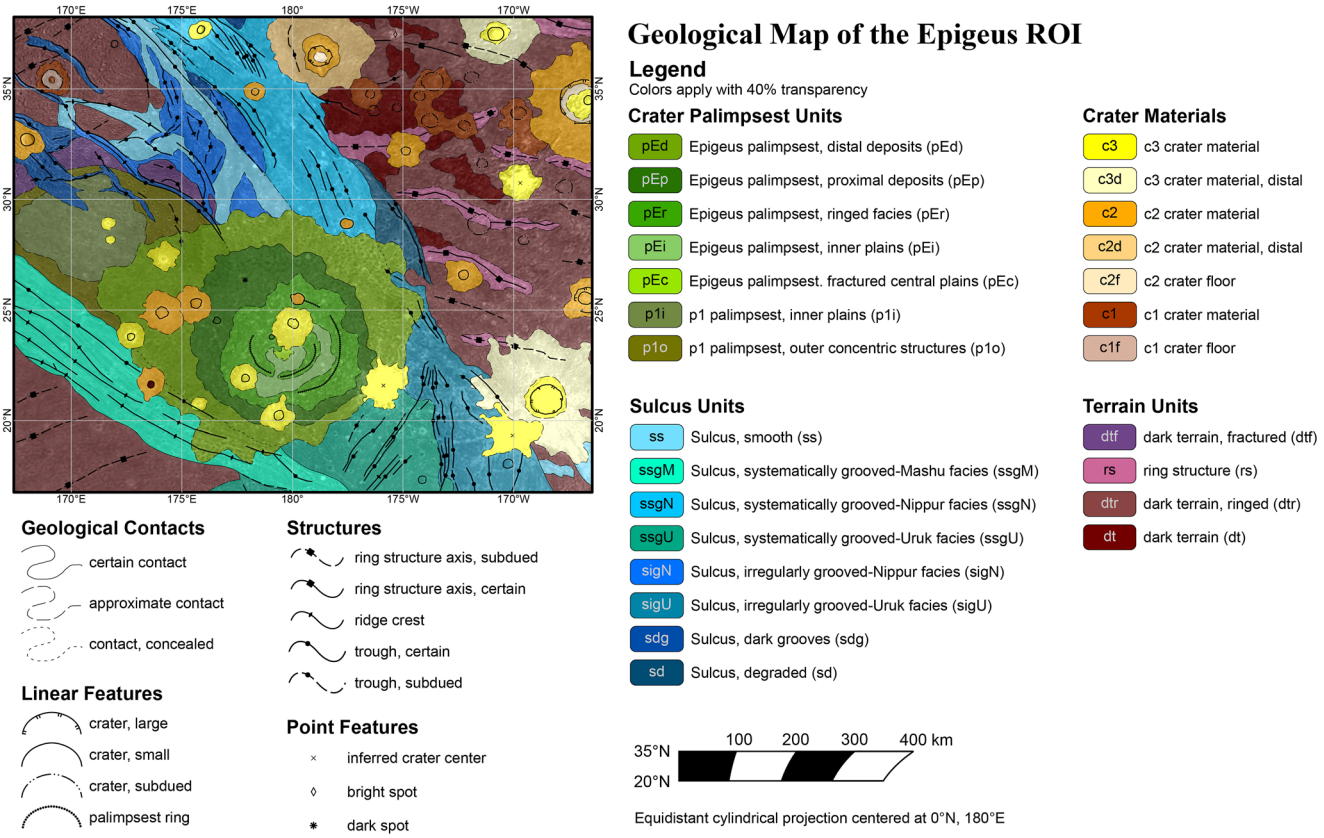

Figure 3. Geological map of the Epigeus Region Of Interest in an equidistant cylindrical projection centered at 0°N and 180°E (see the scalebar for distance variability across latitudes). Units are shown with 40% transparency over the Ganymede controlled basemap (Kersten et al., 2021).

2.3. Geological Mapping

The geological map in Figure 3 displays crater materials and three kinds of geological units divided into sulcus units, palimpsest units, and terrain units. The oldest units are represented by dark terrains (*dt*), often characterized by subdued concentric ring structures (*dtr*). Where the ring structures are more prominent (i.e., Galileo Regio), these are indicated by a separate unit (*rs*). A small portion of dark terrain encompassed between narrow grooved bands is characterized by several systematic fractures and was distinguished as a separate unit (*dtf*). Sulcus units were located on the basis of their morphology, color, and groove direction. The oldest part of the sulci present in the area appears bright yet subdued and poorly grooved (*sd*). The sulcus branches propagating in dark terrains with dark and narrow grooved bands were considered as a separate unit (*sdg*). Sulcus portions showing irregular patterns of grooves were divided into separate facies depending on their location and relative age. In fact, the irregularly grooved Uruk facies (*sigU*) appear morphologically older than the corresponding Nippur facies (*sigN*). Sulcus portions that appear more systematically grooved (i.e., sets of parallel grooves that propagate for large distances) were also divided into facies based on their location and morphological relative age appearance. The systematically grooved Uruk facies (*ssgU*) is older than the Nippur facies (*ssgN*) that looks in turn older than the Mashu facies (*ssgM*). The portions of the sulci where grooves are rarer, less prominent, isolated, or absent, yet appear morphologically smooth and fresh, were mapped as a separate unit (*ss*).

The mapping area encompasses two palimpsests, one of which is very old and subdued; therefore, it is considered as a "*p1*" palimpsest crater. This is characterized by slightly lighter inner plains (p_1i) and outer concentrically fractured plains (p_1o) that blend over the *dtf* unit. The second and youngest palimpsest is Epigeus that, at this mapping scale, could be distinguished into fractured central plain facies (*pEc*), inner plain facies (*pEi*), ringed facies (*pEr*), and proximal deposit facies (*pEp*), where "*facies*" indicate further subdivision of what past works considered as a single unit. Differences between this classification and the high-resolution classification by Jones et al. (2003) mostly depend on the chosen mapping scale that had to be coherent throughout the mapped ROI,

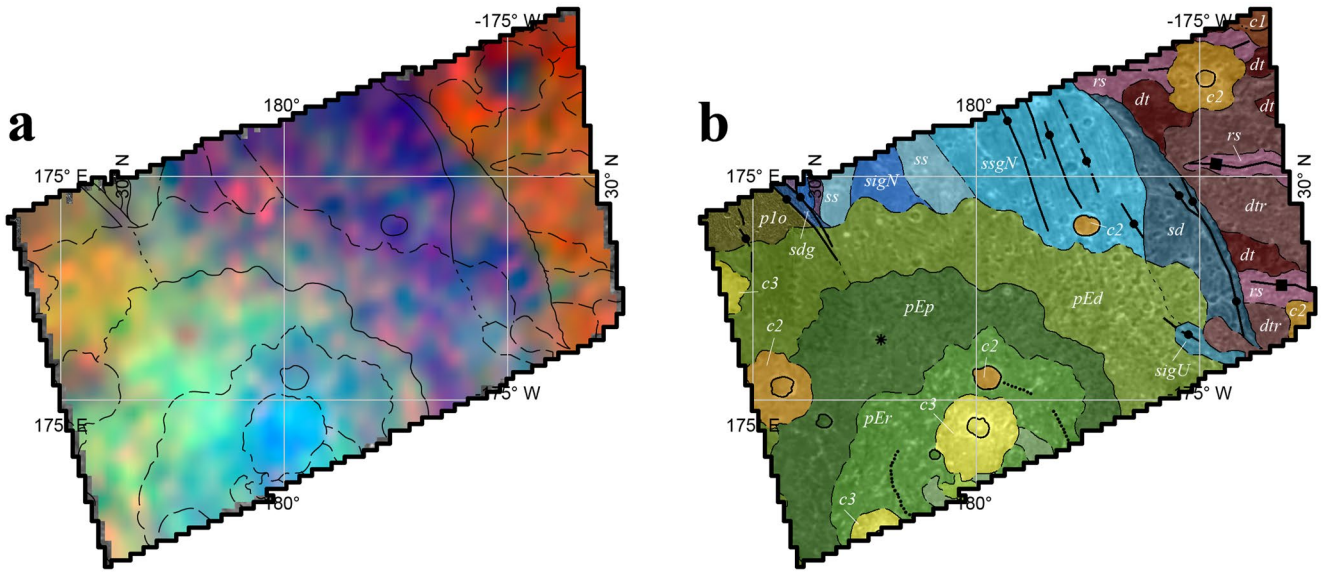

Figure 4. Comparison between Galileo/Near Infrared Mapping Spectrometer (NIMS) data and the geological units. (a) Galileo NIMS *g1g009ci* image rendered with colors R: 4.26 μm (corresponding to the strongest signature of trapped/complexed CO_2); G: 2.02 μm (corresponding to a strong signature of water ice); B: 1.21 μm (near IR continuum) georeferenced onto the reference basemap by Kersten et al. (2021) with overlapped contacts from the geological map in Figure 3; (b) portion of the geological map in Figure 3 (refer to the same figure for the legend).

although we also considered the 90 m/pixel *5481r* to *5521r* SSI frames partially covering the palimpsest to locate the *pEc* facies. Moreover, different from the past geological maps, here we highlight the young stratigraphic position of Epigeus by mapping also the distal deposit unit characterized by numerous secondary craters (*pEd*) mantling the underlying sulcus units.

3. Comparison With Galileo/NIMS Data and Spectral Analysis

We compared our geological map with the Galileo *Near Infrared Mapping Spectrometer* (NIMS) (Carlson et al., 1992) hyperspectral image *g1g009ci*, calibrated in units of radiance factor (I/F) and spanning the spectral range from 0.7 to 5.2 μm, with an average spectral sampling of 25 nm at wavelengths longward of 1 μm. This image covers the southern region of Nippur Sulcus including part of the Epigeus crater at a spatial resolution of 6.7 km/pixel, which is much coarser than the optical basemap. In this hyperspectral image, we first set up a color composite using wavelengths diagnostic of specific compounds (R: trapped/complexed CO_2 at 4.26 μm, G: H_2O ice at 2.02 μm, and B: spectral continuum at 1.21 μm). We observe that the dark terrain units (*dt*, *dtr*) correspond to redder colors, while sulcus units correspond to dark blue to purple colors (see Figure 4). Small craters such as the *c2* crater to the northeast also correspond to bluer colors, hence exhuming an ice phase more similar to the sulcus units. The palimpsest inner and outer facies (*pEc*, *pEi*, *pEr*, *pEp*) correspond to cyan-to-green hues that are well distinguishable from *pEd*, which, in the NIMS data, are noisier and more mixed with the underlying unit colors. The concealed contact with the east, indicating the boundary between Nippur Sulcus and the darker terrains to the west, is covered by a thin layer of *pEd*. NIMS data highlight this contact by showing orange colors to the west of it, also likely due to the overlap of *pEd* on *p1o*. The young *c3* crater to the south corresponds to a bright blue area. The crater excavates the palimpsest center that in turn lies on top of Nippur Sulcus. This is hence a heavily fractured and highly permeable zone where the NIMS data likely highlight a water-rich phase area. By comparison with the dark blue *c2* crater to the northeast, being this *c3* crater the youngest feature in the area, we can assess that bright blue colors correspond to fresher water-rich areas than the dark-blue ones.

Using the whole spectral range of this hyperspectral image, we carried out a spectroscopic analysis aimed at determining the surface composition and some physical properties of the material which makes up the surface regolith. To do so, we first rely on indicators widely used to study the composition and physical properties of water ice-rich surfaces (Filacchione et al., 2012):

- IR slope: computed as the best fit line on the spectral continuum between 1.11 and 2.25 μm, it is mainly correlated with water ice grain size and amount of nonice material.

Table 1
IR Slope and IR Ratio for Pure Granular Water Ice as a Function of Grain Size (Table 3 From Filacchione et al. (2012))

Grain diameter (μm)	$S_{1.11-2.25}$ (μm^{-1})	$\frac{I/F(3.6\,\mu m)}{I/F(1.82\,\mu m)}$
10	−0.125	0.406
30	−0.191	0.232
50	−0.225	0.164
80	−0.257	0.116
100	−0.191	0.096

- 2-μm water ice band depth (BD): derived according to Clark (1999), it is the main indicator of water ice abundance with dependence on grain size distribution and phase angle. However, the hydrated nature of the nonice material can contribute to the depth of the 2-μm band as well.
- The IR ratio between I/F measured at 3.6 and I/F measured at 1.82 μm is a marker for water ice grain size.

For pure granular water ice, the IR slope and IR ratio values as a function of the grain size distribution are known quantities (Table 1).

Because this hyperspectral image was acquired at a given phase angle, we applied no photometric correction, while normalized spectra are sufficient to minimize illumination effects due to local morphology/topography. Individual spectra were then normalized at 0.8 μm before computing spectral indicator values. The results obtained using this method are shown in Figure 5.

The IR slope (Figure 5a) is always negative, running in the −0.45 to −0.21/μm range. The minimum value of the slope is remarkably lower than the values reported in Table 1 probably due to the presence of contaminant species. The IR slope distribution appears anticorrelated with the albedo features, reaching maximum values in the dark terrain units to the east and minimum ones in the bright *c3* crater material overlapped to the Epigeus palimpsest as well as in *c2* crater material to the west.

Different from the IR slope, the 2-μm BD distribution (Figure 5b) is strongly correlated with albedo, resulting in higher values in bright material and lower in the dark terrain. This may be due to larger amounts of water ice in the bright areas.

An indication of the distribution of the water ice-rich grains in the surface regolith can be derived by means of the IR ratio (Figure 5c): the lowest values of this ratio (∼0.10, black color) found in the bright *c3* crater material and other smaller spots in its neighborhood correspond to grains as large as 100 μm, while the highest values of the IR ratio (∼0.20, white color), correlated with dark terrain units, indicate finer grains.

The three spectral indicators can be merged into a single color composite image with the IR slope rendered in red color, the 2-μm BD in green, and the IR ratio in blue (Figure 6). In this color scheme, and in the hypothesis of a water ice-dominated surface, areas in green are characterized by a high albedo, large regolith grains (100s μm), and stronger water ice band, whereas areas in magenta are associated with dark terrain units where the 2-μm water ice band is shallower and the ice grain size is smaller (10s of μm). The different grain sizes in the same area, undergoing similar space weathering effects, could be explained by the fact that grooved terrains and dark terrains have substantially different ages. The blue color is associated with the center of the *c2* crater material, where the IR slope is remarkably lower and the 2-μm BD is higher than the nearby ejecta field.

Figure 7 shows the average I/F spectral profiles for the main compositional units found in the NIMS hyperspectral image *g1g009ci*. All classes show the diagnostic absorptions of water ice at 1.05, 1.25, 1.5, 2.05, and 3.0 μm. The 1.65-μm feature, observed in all spectra, is a strong indicator of crystalline water ice. A small band centered

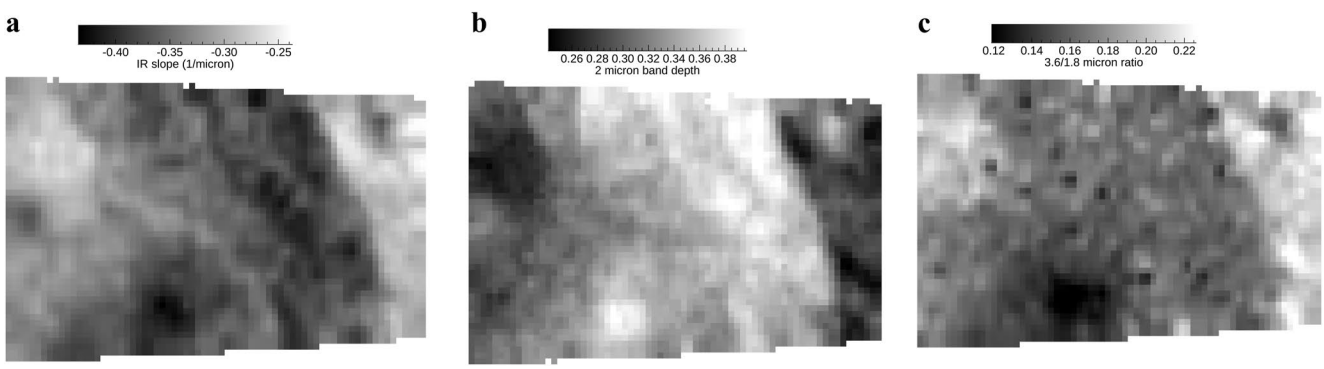

Figure 5. Spectral indicators computed based on the Near Infrared Mapping Spectrometer hyperspectral image *g1g009ci* covering the southern region of Nippur Sulcus: IR slope (panel (a)), 2-μm water ice band depth (panel (b)), and IR ratio (panel (c)). Data are projected using the Albers equal-area projection.

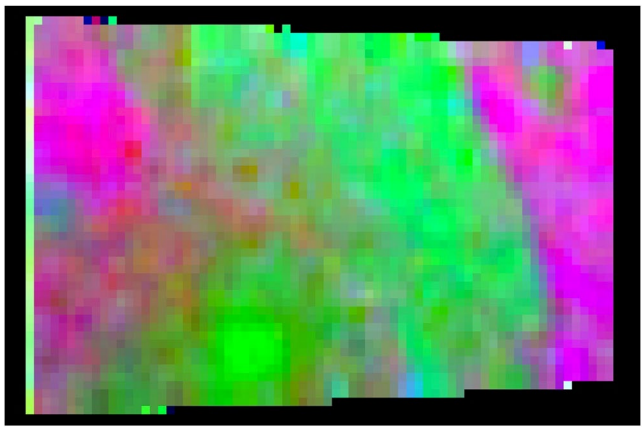

Figure 6. Color composite map of the spectral indicators (R: IR slope, G: 2-μm water band depth, B: IR ratio) computed on the Near Infrared Mapping Spectrometer hyperspectral image *g1g009ci* and covering the southern region of Nippur Sulcus.

between 3.2 and 3.3 μm is also evident, potentially due to organic compounds (McCord et al., 1997). The trapped/complexed CO_2 feature at 4.26 μm shows up both in the *c2* and *c3* impact craters and in the dark terrain, but it is very weak, preventing a mapping of the strength of this spectral signature.

Modeling of near-infrared spectra is a complicated task because the mixing of volatile ices (mostly water and carbon dioxide) with non-ice materials such as hydrated salt minerals, sulfuric acid hydrate, organics, and possibly phyllosilicates, whose existence on the surface of Ganymede was suggested by previous literature, is a strongly nonlinear process. As demonstrated by laboratory experiments, the mixing processes occurring in water and hydrated salt solutions at cryogenic temperatures are characterized by a complex chemical and regolith phenomenology, where new bonds and absorption features may arise as a function of the temperature (Fulvio et al., 2023).

A safe identification of non-ice species in NIMS spectroscopic data is challenged by several concurring effects: (a) the spatial resolution of NIMS data is quite coarse in absolute terms; (b) the spectral sampling of NIMS data is low and does not allow one to resolve the narrowest spectral signatures of several non-ice compounds; (c) the optical constants of some non-ice materials are not yet available; and (d) the surface of Ganymede is altered by the interaction with magnetospheric particles and by thermal evolution of the regolith grains.

Given the complexity of the chemistry, several authors have based their analyses on pure water ice properties for a first investigation of high albedo units, such as young impact craters (e.g., Lucchetti et al., 2023). For low albedo units, several attempts have been made to model Ganymede's reflectance spectra by adopting a linear mixing of water ice and non-ice species (e.g., King & Fletcher, 2022; Ligier et al., 2019; Stephan et al., 2020). In this way, new spectral indicators can be qualitatively defined for several linear mixtures as a function of the relative abundances and grain size. As an example, Stephan et al. (2020) derived the trends of the 2.0/1.5, 2.0/1.25,

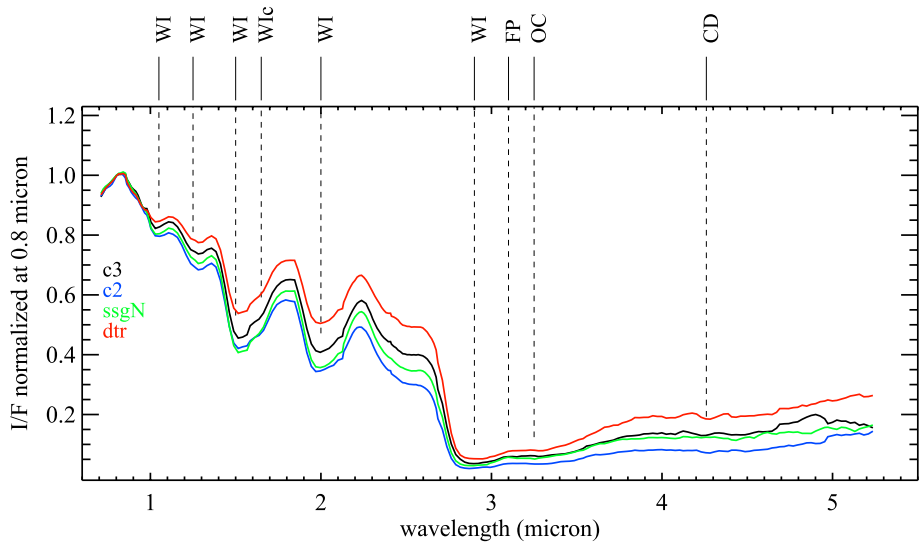

Figure 7. Average spectral profiles of the geologic features *c3* (black), *c2* (blue), *ssgN* (green), and *dtr* (red) derived from the Near Infrared Mapping Spectrometer (NIMS) hyperspectral image *g1g009ci*. Each spectral profile result from the average of 4 (2 × 2) pixels centered on the geologic feature of interest. The labels on the top axis respectively identify Water Ice, Water Ice in Crystalline form, water ice Fresnel Peak, Organic Compounds, and Carbon Dioxide. A boxcar smoothing function ×3 was applied to cancel or reduce noise-induced features (*spikes*). Spectra were normalized at 0.8 μm to minimize photometric effects and allow comparisons. A rough evaluation of the signal-to-noise ratio of NIMS data is provided by Greeley et al. (2009), who reported a value of 5–50. The instrumental noise varies along the spectral range and depends both on instrumental parameters (e.g., integration time, operating temperatures) and external circumstances (illumination and viewing geometries) that change from one observation to another (Carlson et al., 1992).

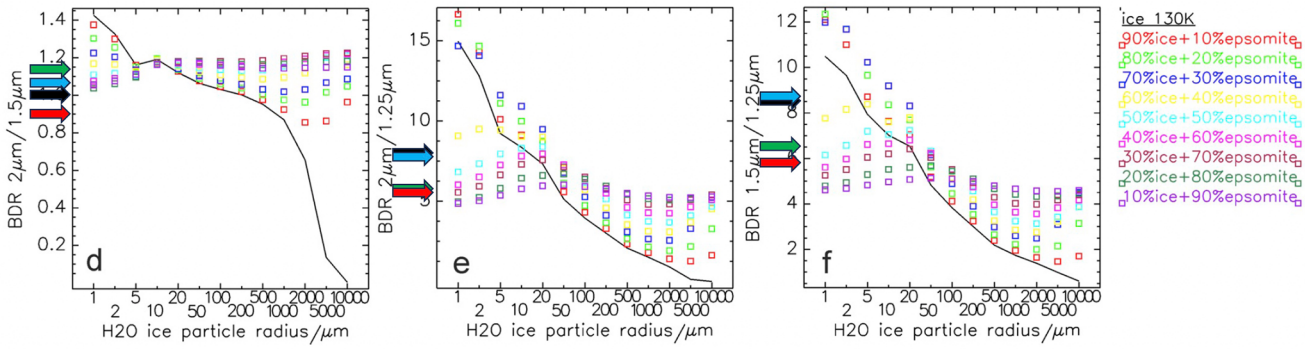

Unit	BD(1.25)	BD(1.5)	BD(2.0)	BD(2.0)/BD(1.5)	BD(2.0)/BD(1.25)	BD(1.5)/BD(1.25)
c3	0.04	0.34	0.34	1.0	8.5	8.5
c2	0.04	0.35	0.33	1.06	8.25	8.75
ssgN	0.06	0.39	0.34	1.14	5.7	6.5
dtr	0.05	0.29	0.26	0.9	5.2	5.8

Figure 8. Top: theoretical trends of water ice and epsomite mixtures (Figures 6d–6f from Stephan et al., 2020) from which the grain radius can be derived. The solid black line corresponds to the theoretical band depth ratios (BDR) trends for pure granular water ice as a function of the grain radius. The colored arrows on the left edge of the ordinate axis indicate the value of the BDR-values estimated for *c3* (black), *c2* (blue), *ssgN* (green), and *dtr* (red) units, respectively. Bottom: table summarizing the band depth and BDR-values measured on the *c3*, *c2*, *ssgN*, and *dtr* units.

and 1.5/1.25 μm band depth ratios (BDR) for several mixtures of water ice plus carbon (C), magnetite (Fe_3O_4), pyrrhotite (FeS), serpentinite and epsomite ($MgSO_4 \cdot 7H_2O$), with grain sizes between 1 μm and 1 cm. Except for epsomite, a hydrated magnesium sulfate salt whose presence had originally been suggested on Ganymede's surface, all simulated mixtures show a general departure of the above ratios from the case of pure granular water ice. This departure is a function of both the abundance of the contaminant and the grain size.

The trends are more complicated for epsomite, given its hydrated nature: when the epsomite concentration is small (10%), the BDR values are almost unperturbed compared to pure water ice, whereas at higher concentrations the values of the ratios become significantly higher for grain sizes larger than 20 μm and lower for grain sizes smaller than 10 μm. In Figure 8 we report the values of the BD for the water ice absorption bands centered at 1.25, 1.5, and 2.0 μm, and the 2.0/1.5, 2.0/1.25, and 1.5/1.25 μm BDRs, computed on the spectra of the ROIs tagged *c3*, *c2*, *ssgN*, and *dtr*, respectively. In the same figure, we show BDR values with respect to the similar quantities computed for a mixture of water ice and epsomite at different grain sizes from Stephan et al. (2020).

The 2.0/1.5 μm BDR for *ssgN* and *c2* spectra is compatible with any grain size between 1 μm and 1 cm and 30%–60% epsomite abundance. We note a degeneration of the theoretical curves at ∼10 μm grain size. The *c3* and *dtr* spectra are compatible with grains larger than 500 μm and with ≤30% abundances of epsomite.

The 2.0/1.25 and 1.5/1.25 μm BDR values group together the *c3*–*c2* and *ssgN*-*dtr* spectra: the former are compatible with 5–20 μm grains with an epsomite abundance of about 30%–60%, while the latter are compatible with grains smaller than 50–100 μm and abundances of about 50%–60%. Given the similar nature of the craters, the consistency between the *c3* and *c2* spectral indicators is reasonable. On the other hand, from a geologic and photometric perspective, the similarity of the spectral indicators on the Nippur facies (*ssgN*) and the dark terrain unit (*dtr*) is hard to explain.

These results demonstrate how complicated it is to find convergent solutions with spectral indicators based only on a few specific spectral features: as an example, the *c3* and *dtr* ROIs are compatible with very large grains (≥500 μm) from their 2.0/1.5 μm BDR value, whereas their 2.0/1.25 and 1.5/1.25 μm BDR values are consistent with much smaller grains (<5–20 μm). These apparent inconsistencies can be resolved only through the application of a thorough spectral modeling on high-spatial- and high-spectral-resolution data, which is a task for future close exploration.

4. Nippur Sulcus Grooves' Analysis

The tectonic activity characterizing Ganymede's evolution is largely inferred from the presence of grooves on the surface of the icy satellite. Indeed, grooves are regional scale morphotectonic structures, from linear

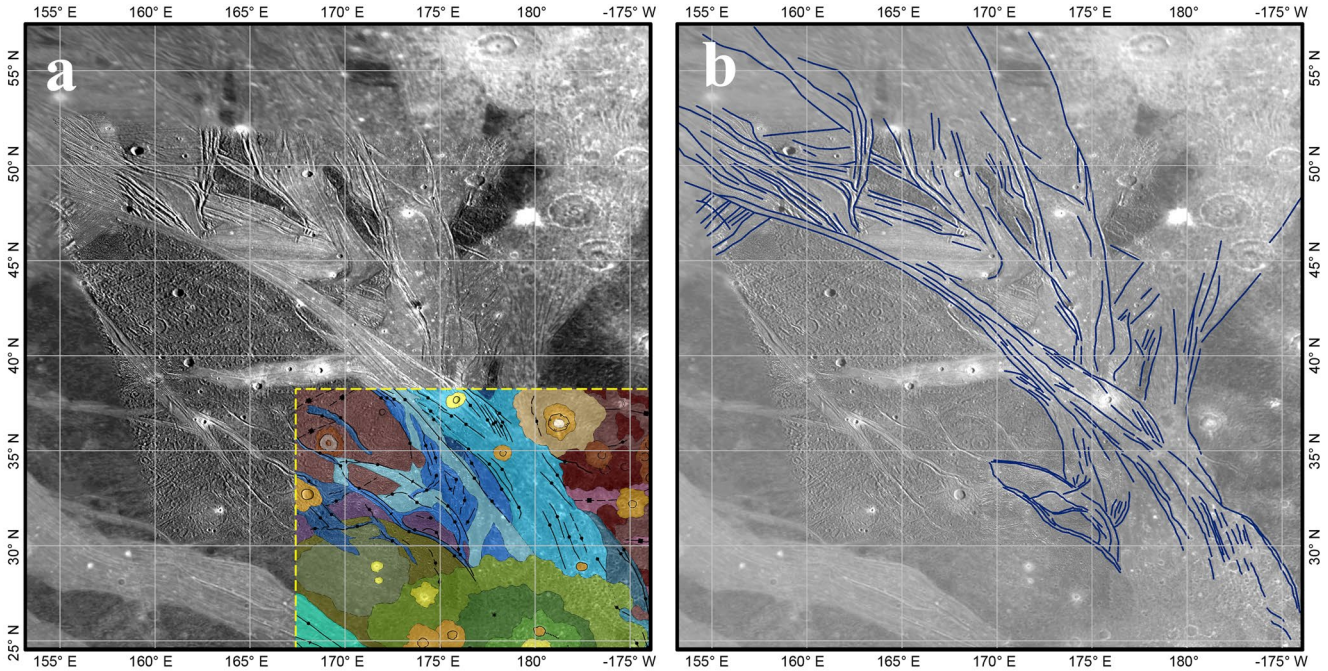

Figure 9. Nippur Sulcus area just north of the Epigeus Region Of Interest (ROI) as shown in the controlled Ganymede basemap by Kersten et al. (2021). (a) Mapping area extent and location of the Epigeus ROI (Figure 3); (b) Mapped grooves updated from Rossi et al. (2020) and georeferenced onto the controlled basemap.

to curvilinear, expressing the brittle deformation of the light terrain (Bianchi et al., 1986; Lucchitta, 1980; Pappalardo & Greeley, 1995; Pappalardo et al., 1998, 2004). In addition, grooves may have acted as conduits in the possible connection between the surface and subsurface ocean (Head et al., 2002). The investigation of the main properties of fault populations on icy satellites allowed to constrain the depth at which fractures penetrate within the icy layer, such as in the Enceladus and Ganymede cases (Lucchetti et al., 2017, 2021). Here, we study the trend of the groove length and spatial distribution (Bonnet et al., 2001; Bour & Davy, 1999; Bour et al., 2002; Gudmundsson et al., 2013) of the Nippur Sulcus region to estimate the potential thickness of the icy crust. The Nippur Sulcus area is centered at 40°N and 170°E and displays tectonic deformation due to both extensional and strike-slip regimes (Cameron et al., 2018). This area, located north of the ROI, provides adequate grooves to estimate the potential thickness of the icy crust intersected by groove penetration near the Epigeus palimpsest, considering that at least 50 fractures are needed for a good statistic.

We improved the regional scale groove mapping of Rossi et al. (2020), where grooves were identified as topographic expression of trough structures whose bottom is identified by a contrast in brightness depending on the illumination conditions (Figure 9). First, the grooves detected by Rossi et al. (2020) were mapped on the global image mosaic of Ganymede with a resolution of 1 km, assembled by the USGS Astrogeology Science Centre (Becker et al., 2001). The selected grooves from this data set and located in the Nippur Sulcus area were updated, improved and georeferenced to the new controlled 359 m/pixel global Ganymede mosaic from Voyager and Galileo images by Kersten et al. (2021), allowing the detection of a larger number of features. Ganymede's grooves were mapped on different types of light material units: light irregular material, light subdued material, light grooved material, and undivided light material, following the nomenclature of the latest Ganymede geological map (Collins et al., 2013). The total number of grooves mapped in this work is about 200 (Figure 9).

On this data set, we applied both a length distribution and a self-similar clustering analysis to give new insight into the vertical propagation within the Ganymede icy shell. Fault size and spatial distribution can be statistically investigated, in terms of length and clustering, to provide new insights into deformation rates, stress transmission modes, rheology of the medium, and mechanical layering (Benedicto et al., 2003; Gudmundsson, 2012; Gudmundsson et al., 2010, 2013; Schultz et al., 2010; Soliva & Schultz, 2008). The length distribution analysis describes the propagation and confinement of a groove system. Indeed, the vertical dimension of a fault (height), which is proportional to fault length, is governed by the mechanical layering of the crust (e.g., Benedicto

et al., 2003; Gudmundsson et al., 2010; Soliva & Schultz, 2008). In this context, faults' length analysis foresees two endmembers (e.g., Schultz et al., 2010; Soliva & Schultz, 2008): (a) fault populations characterized by a negative exponential length distribution, which are regularly spaced and confined in depth (e.g., Ackermann et al., 2001; Cowie et al., 1994) and (b) fault populations characterized by a power law length distribution, which presents few large, separated faults cutting the whole crust.

In the Nippur Sulcus area, the length distribution analysis displays both behaviors (exponential and power law) reflecting the presence of both fault populations. Grooves with a length smaller than 152 km (about 130 grooves) are well modeled by an exponential distribution, while grooves with a length larger than 152 km (about 70 grooves) are best fitted by a power-law distribution (Figure 10). The exponential fit model well represents the beginning phase of fracture propagation, when the nucleation of new faults takes place and mechanical layering is negligible (Ackermann et al., 2001; Cowie et al., 1994; Schultz et al., 2010), while the power law model well illustrates the grooves' interaction and the following linkage/growth process (Cowie et al., 1994).

We then applied the self-similar clustering analysis (Bonnet et al., 2001; Mazzarini, 2004) on the Nippur Sulcus grooves to determine how fractures fill space (i.e., fracture spatial distribution). In this way, we determine the vertical propagation of the fracture network and evaluate the scaling properties of the system (Mazzarini & Isola, 2010). We applied the self-similar clustering analysis considering the two-point correlation function method to measure the fractal dimension of the fracture population for an interval of lengths (the size range) falling between a lower and an upper cutoff (L_{co} and U_{co}, respectively, see Lucchetti et al. (2021) for details on method explanation). While L_{co} is not reliable due to data noise, U_{co} reflects the vertical maximum propagation of the fracture network (Mazzarini & Isola, 2010; Mazzarini et al., 2013); hence, it depends on the mechanical layering of the medium. Our findings determine that the vertical extension for the Nippur Sulcus region ranges between 125 and 135 km, suggesting that this limit might be the probable thickness of the icy crust located above the ocean (Figure 11). This result is in good agreement with previous Ganymede results that found an icy crustal thickness of 100–130 km in the equatorial regions of the satellite (Lucchetti et al., 2021), and in addition, it is similar to what was previously found from independent analysis (icy shell thickness from 80 to 150 km, Kivelson et al., 2002; Saur et al., 2015; Schenk, 2002).

Although we cannot retrieve the time evolution of faults, we can suggest the following formation scenario: at the beginning, the crust underwent deformation by large faults that cut across the entire icy crust down to the ocean interface. Then, over time, minor deformations contributed to the development of faults following an exponential distribution and cutting the crust down to the brittle-ductile interface (Lucchetti et al., 2021). This interpretation may suggest that the groove development originated from synchronous extension and strike-slip

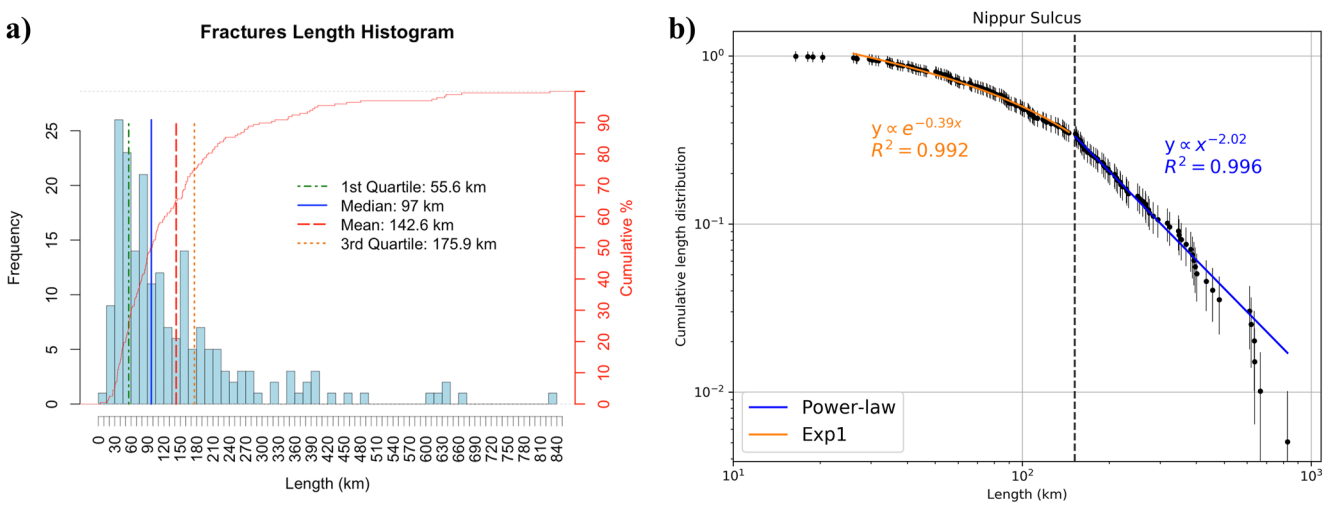

Figure 10. (a) frequency histogram of all grooves identified in Figure 9. The main statistical properties of the right-skewed distribution are also indicated in the figure. (b) Cumulative length distribution of the data set, where the vertical error bars indicate the root of the cumulative number of counting fractures. The fitting models of cumulative length distribution are shown on the graph: grooves shorter than the threshold length *Lth* (black dashed vertical line, in this specific case *Lth* = 152 km) are fitted by exponential distributions (orange curve), while grooves longer than *Lth* are fitted by a power-law distribution (blue curve).

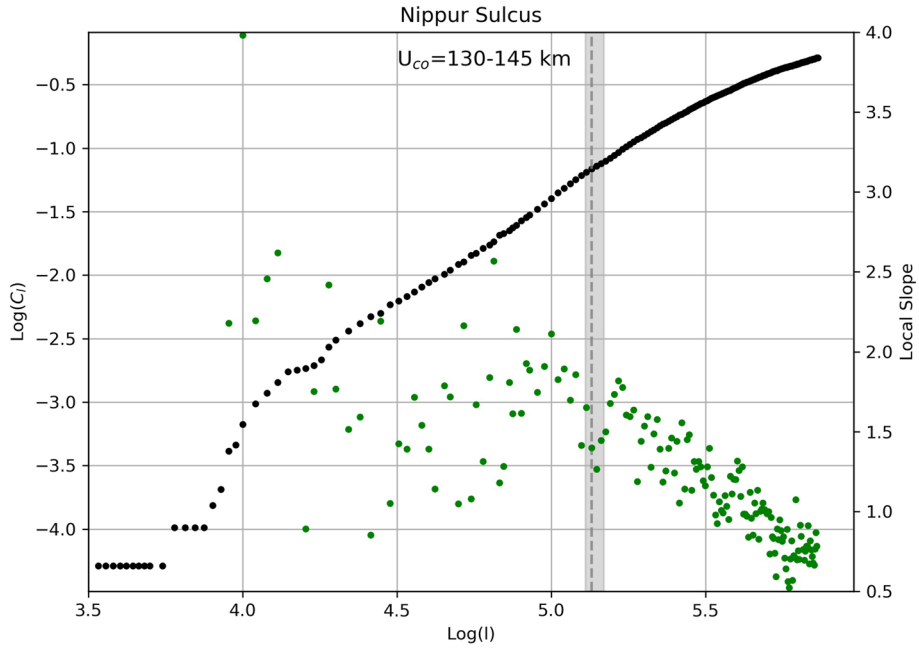

Figure 11. Self-similar clustering investigation for Nippur Sulcus. Here, we report the log plot of the correlation function versus groove length ($C(l)$ vs. l, black points) and the *local slope* ($\Delta\log(C(l))/\Delta\log(l)$) versus Log($l$) plot (green dots). The length interval of interconnected grooves is represented by the plateau stage of the local slope curve (green dots). The gray stripe displays the U_{co} interval defining the length interval of the fractal distribution. The slope of the curve (black dots) is the fractal exponent D (equal to 1.6) calculated in the length interval $L_{co} - U_{co}$. The fractal distribution endsì when the local slope curve (green dots) breaks. The breaking point corresponds to a Log(l) value (U_{co}) that reflects the potential thickness of the icy shell above the subsurface ocean required for the development of densely populated features at the surface (i.e., the grooves).

deformation through time, even though a structural analysis at a higher spatial resolution is pivotal to provide a proper explanation.

5. Simulations of the Clutter Noise Expected in Nippur Sulcus

Operating at a central frequency of 9 MHz and transmitting either a 3 or 1-MHz bandwidth (corresponding to a range resolution in water ice of about 30 and 90 m respectively), the *RIME* (Bruzzone & Croci, 2019) is tasked to explore the subsurface of Ganymede, Europa and Callisto down to a depth of few kilometers (Bruzzone & Croci, 2019; Bruzzone et al., 2011). The potential for the identification of liquid water, and thus of a potential habitat, beneath the crust of the Galilean icy satellites, makes RIME one of the key experiments of JUICE. Orbital subsurface sounding radars (radar sounders) such as RIME have been successfully flown to the Moon (Ono et al., 2009; Phillips et al., 1973) and Mars (Fan et al., 2021; Picardi et al., 2005; Seu et al., 2007). They work by transmitting electromagnetic pulses at frequencies in the MF, HF, and VHF ranges of the radio spectrum into the surface of a planet or satellite to detect reflected signals from subsurface structural or compositional interfaces.

The electromagnetic pulse can also be scattered by rough topography. Topographic roughness of the surface of a body illuminated by the radar produces secondary echoes in addition to the one caused by the surface closest to the radar. These echoes are produced by portions of an irregular surface that are oriented so as to have near-normal incidence with respect to the direction pointing to the spacecraft. As these echoes originate away from the ground track of the spacecraft, they reach the radar after the primary nadir reflection, and can be mistaken for subsurface echoes, thus complicating the interpretation. This phenomenon is dubbed "*clutter*."

To validate the detection of subsurface interfaces, numerical electromagnetic models of surface scattering have been used to produce simulations of surface echoes (e.g., Ilyushin et al., 2017; Nouvel et al., 2004; Russo et al., 2008; Spagnuolo et al., 2011) that are then compared to real echoes detected by the radar to distinguish between surface clutter, which should be present both in real data and simulations, and genuine subsurface

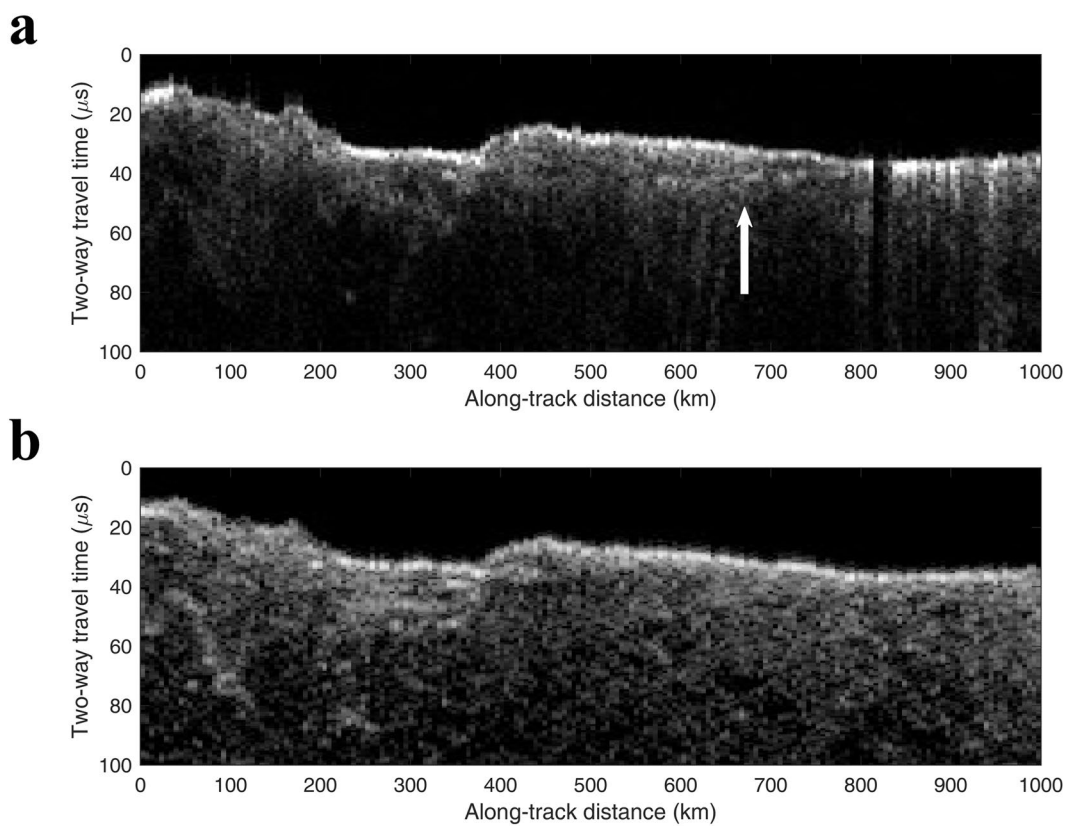

Figure 12. Comparison between (a) real and (b) simulated radargrams for MARSIS orbit 4011 (see text for details). The simulation reproduces echoes from topography only, while real data contain both surface and subsurface echoes. The arrow highlights a weak subsurface reflection (from Orosei et al. (2017)).

reflections, which show up only in actual measurements. This procedure is illustrated in Figure 12, comparing a real and a simulated radargram for the MARSIS radar sounder at Mars (Picardi et al., 2004) during orbit 4011 of the ESA Mars Express spacecraft (Chicarro, 2002). A radargram is a visualization of radar signals recorded in succession as the sensor moves along its trajectory. The along-track distance is represented by the *x*-axis, while the *y*-axis records the round-trip delay of an echo sample and the power of the signal is represented by the brightness of the pixel.

Information available on the topography of Ganymede, as well as on other Galilean satellites, is based on stereo processing of Voyager and Galileo images (e.g., Berquin et al., 2013; Leonard et al., 2020; Lesage et al., 2021; Schenk, 2009; Steinbrügge et al., 2020; Zubarev et al., 2017). Unfortunately, the availability of stereo pairs for Ganymede is limited, and the resolution of the resulting digital elevation models (DEMs) is of the order of a few to several hundred meters or more. None of the available stereo DEMs covers the Nippur Sulcus region, so we had to build a synthetic topographic model based on a single high-resolution image of an area centered at 30°N, 174°E (Galileo/SSI image *2400r*, 189 m/pixel).

We started from the assumption that in a relatively small portion of the Ganymede surface and at a given local daytime, differences in the observed reflectance are largely due to differences in topographic reliefs rather than differences in albedo, that is, chiaroscuro is dominated by topography rather than by the intrinsic reflectivity of the surface. Using ISIS3, we then modeled shadings as observed in calibrated images to simulate pixel-by-pixel reliefs using the formula:

$$D = \left(\text{I\_F} * R^2/1000\right) - R \quad (1)$$

where I_F is the radiance factor I/F, and $R = 2{,}631.2$ km is the equatorial radius of Ganymede.

After calculating D, to prepare the synthetic topographic model (hereafter DEM, for simplicity), we applied the following steps:

1. Application of "algebra" function to scale the simulated reliefs to the Ganymede radius:

$$D_r = (A * D) + C \quad (2)$$

where A and C are two constants (in this specific case, $A = 1$ and $C = R = 2{,}631.2$).

2. The application of "*demprep*" function is necessary for the preparation of a DEM file so that it can be used as a shape model.
3. The application of "*shade*" function to create a shaded-relief cube from a topographic cube.
4. Application of *cam2map* to project the synthetic topographic model in an equirectangular projection.

In the present work, we use a numerical code based on the model by Nouvel et al. (2004), together with this synthetic DEM, to compute the size and orientation of the discretized topography modeled as a set of rectangular facets that are smooth rectangular areas representing the surface of the planet between four adjacent points in the DEM, coherently scattering toward the radar. Although such a representation of topography is a highly idealized one, it has been shown that it is adequate to model surface scattering provided that the height deviation of the real topography from the smooth facet is about half a wavelength (Nouvel et al., 2004), which for RIME ranges between approximately 30 and 40 m. A full three-dimensional model of propagation in the subsurface of Ganymede, such as the one presented in Heggy et al. (2017), is outside the scope of this work. The present approach, although simpler and narrower in scope, aims at providing a direct assessment of surface clutter in different areas of Ganymede, and at producing synthetic radar data on which clutter reduction schemes can be tested.

The model by Nouvel et al. (2004) is just one of many representations of the scattering from a discrete, regular surface element found in the literature, but it has proven its value in several applications related to the interpretation of radar sounder data (see e.g., Mouginot et al., 2009, 2010, 2012). The assumption at the base of the model is that scattering of electromagnetic waves takes place predominantly at the surface. However, Earth-based radar observations of the icy Galilean satellites at centimetric wavelengths yield values of the radar cross section exceeding unity, with high polarization ratios and a diffuse scattering law that are unlike the quasi-specular reflections observed in terrestrial planets and the Moon (Black, Campbell, & Nicholson, 2001). These characteristics were interpreted by Black, Campbell, and Ostro (2001) as due to coherent backscatter from scatterers embedded in the weakly absorbing water ice rather than single scattering from the vacuum–surface interface. Their model was able to reproduce the data for a distribution of scatterer size following a power law with an exponent between −3.5 and −4, and a maximum size of scatterers of about 1 m or less. However, such embedded scatterers are at least one order of magnitude smaller than the wavelength of RIME, and thus have minimal influence on the propagation of radar waves at RIME frequencies (e.g., Stratton, 1941). For this reason, we model scattering from the surface of Ganymede as caused by reflections at the vacuum–surface interface. More recently, an alternative explanation for the unusual radar properties of Europa has been proposed by Hobley et al. (2018) who modeled the sublimation of ice at the surface to find that it could produce the formation of vertical blades of ice up to several meters high. The occurrence of such formations is determined by the relative speed of ice sublimation and diffusion processes smoothing ice topography and can thus be specific for the conditions of Europa. We note however that if such a surface morphology was present on Ganymede, a different surface scattering model, presumably a non-coherent one, would be required.

In the present study, the resolution of the DEM employed in the simulations is approximately 190 m, and the ratio of DEM resolution to RIME wavelength is between five and six, in the same range as the ratio between the MARSIS wavelength and the MOLA global topographic data set (Smith et al., 2001) used to simulate scattering from the Martian surface (Nouvel et al., 2004). The statistical properties of the DEM employed in scattering simulations are shown in Figures 13a–13c. While the range of topographic heights is in line with what is expected for Ganymede (e.g., Zubarev et al., 2017), slopes appear to be much steeper than in previous studies (a median slope of 23° for a 190 m baseline compared to values well below 10° for a baseline of 630 m in Berquin et al. (2013)). As this characteristic may be an artifact of our synthetic DEM processing, we decided to also perform simulations for the same DEM in which topographic heights are scaled to 1/3 of their original values: the resulting median slope is about 8° for a 190 m baseline, while the corresponding histograms of heights and slopes are also shown in Figures 13d–13f.

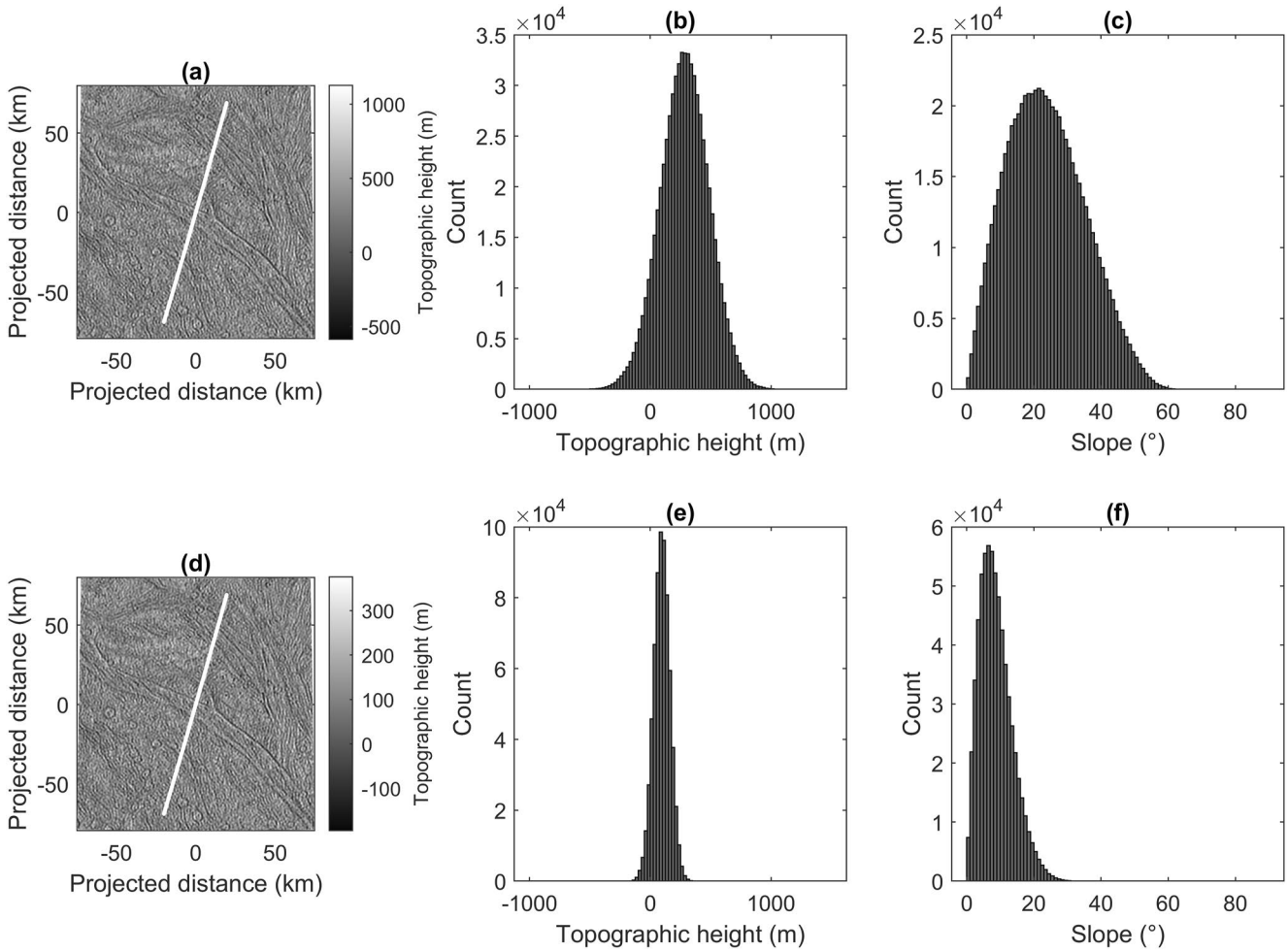

Figure 13. Properties of the synthetic digital elevation model (DEM) used in the simulation of surface scattering at Radar for Icy Moon Exploration frequencies. (a) Gray-scale relief representation of the DEM resulting from the processing described in the text, with the ground track of the simulated spacecraft trajectory shown in white. (b) Histogram of topographic heights of the DEM in panel (a). (c) Histogram of bidirectional slopes of the DEM in panel (a). (d) Same as (a) but topographic heights have been reduced by a factor of 3 (see text for details). (e) Histogram of topographic heights of the DEM in panel (b). (f) Histogram of bidirectional slopes of the DEM in panel (d).

The discrepancy between statistical properties of topography in the present work and that of studies such as Berquin et al. (2013) can result from many factors, not the least of which is the method used to derive topography from images. A comparison between DEMs of different areas obtained through different methods would require a test to verify that the same images processed in different ways produce DEMs with similar properties. Such a comparison would certainly provide useful insight into the limitations of simulations in predicting surface scattering at RIME frequencies, but it is a complex task deserving perhaps a dedicated work in itself.

Surface scattering simulations have been run for 200 pulses along the ground track shown in Figures 13a and 13d. The resulting radargrams are plotted in Figure 14. Because of the limited size of the DEM, simulated echoes end abruptly between 90 and 200 μs after the beginning. For this reason, radargrams have been cropped to show only the first 70 μs, corresponding to the two-way travel time of an electromagnetic wave in ice to a depth of 6 km. A qualitative comparison with Figure 12, neglecting the difference in frequency between MARSIS and RIME, reveals that surface clutter decays much more slowly for a Ganymede-like topography. This is presumably due to its higher roughness, producing a distribution of orientations for the discrete facets modeling the topography in which a significant fraction of them can scatter nearly specularly toward the radar for a wide range of distances from the nadir. Further examination of Figure 14 also shows that clutter on Ganymede appears to be a nearly random process, exhibiting no recognizable feature related to the surface morphology producing it (see Figures 13a and 13d). Qualitatively, there appears to be no difference between simulations run for the original

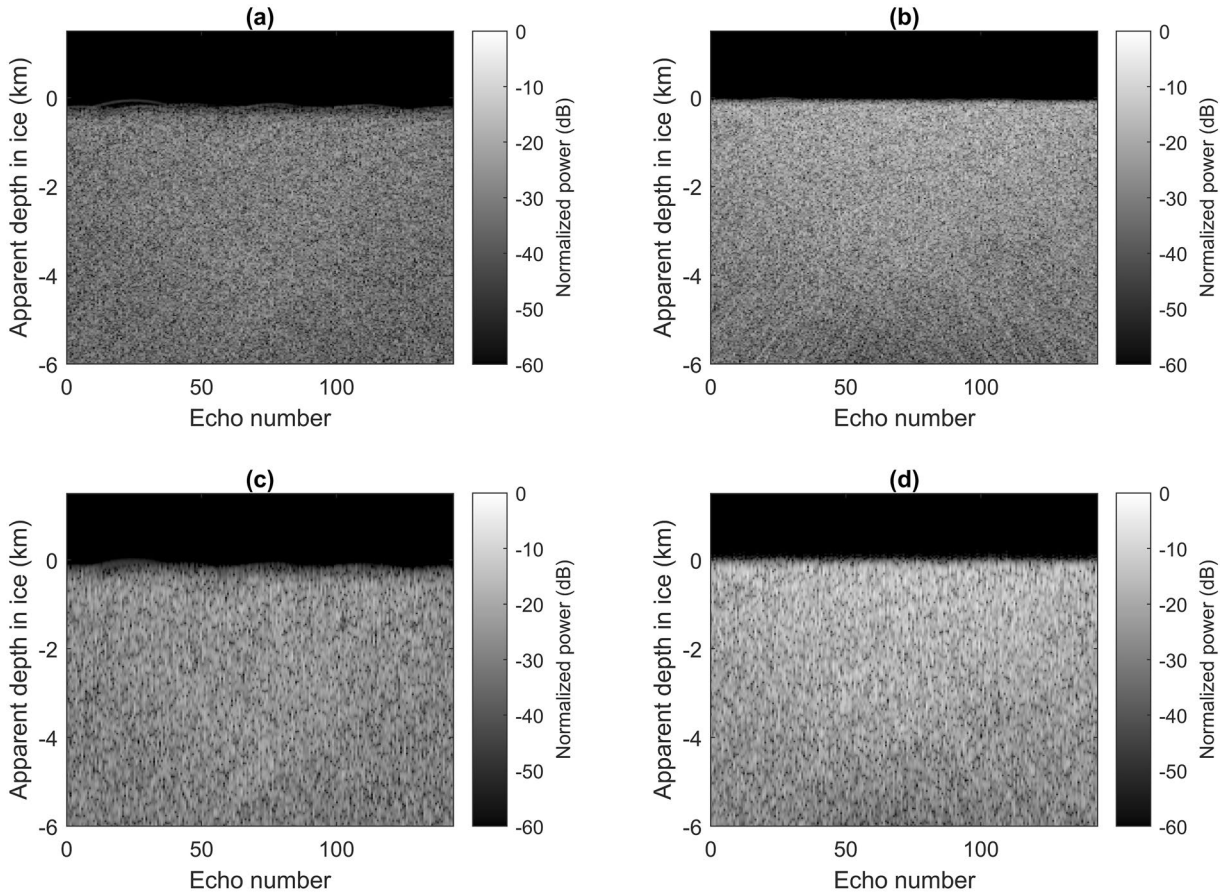

Figure 14. Radargrams of simulated surface echoes produced using the digital elevation models (DEMs) are shown in Figure 13. The time delay of echoes has been converted to the depth in water ice from which a radar echo would have the same time delay. Echoes have been filtered using a Hamming window to reduce sidelobes. The radargrams have been cropped to show only the part of the echoes that is not affected by the finite size of the DEMs. (a) Radargram for a 3 MHz bandwidth pulse for the DEM in Figure 13a. (b) Radargram for a 3 MHz bandwidth pulse for the DEM in Figure 13d. (c) Radargram for a 1 MHz bandwidth pulse for the DEM in Figure 13a. (d) Radargram for a 1 MHz bandwidth pulse for the DEM in Figure 13d. In all four radargrams, surface echoes have a diffuse appearance without recognizable features connected to topography, both for the original version of the DEM and for the one in which heights have been scaled down to 1/3, and irrespective of bandwidth.

version of the DEM and the one in which heights have been scaled down to 1/3, and neither pulse bandwidth seems to influence clutter characteristics.

The trend of clutter noise as a function of the depth of a potential subsurface echo can be observed in Figure 15, which shows plots of the median surface echo for different versions of the DEM and different bandwidths. The plots are normalized to the power of the echo from a flat surface for reference. All echoes have been filtered by means of a Hamming window, as it is done in MARSIS and SHARAD data processing, to suppress sidelobes (Harris, 1978). As it could already be gleaned from Figure 14, the rate of decay of clutter noise with depth is low, although the power of the diffuse echo is 15–20 dB below that of a specular reflection. As expected, the decay rate of clutter for the scaled DEM is greater than that for the original DEM (about 3 vs. 1 dB/km), but the power of clutter for the smoother DEM is also higher. The clutter power curves for the two DEMs intersect towards the end of the depth interval considered in the analysis of results. It is reasonable to assume that for depths greater than the 6 km covered in this study, clutter noise from the rougher original DEM will be higher than the one from the smoother re-scaled version. As the goal of the RIME experiment is to probe the subsurface of Galilean satellites down to a maximum depth of 9 km (Bruzzone & Croci, 2019; Heggy et al., 2017), clutter from rougher terrains will affect the detectability of deeper, weaker reflections from the subsurface. It can be seen in Figure 14 that clutter for a 1-MHz-bandwidth pulse is greater than the one for the 3-MHz bandwidth, when compared to a specular reflection. This effect is due to a greater decrease in echo power for a coherent echo than for a diffuse one when bandwidth is narrowed. Decreasing the bandwidth of a specular reflection from 3 to 1 MHz decreases

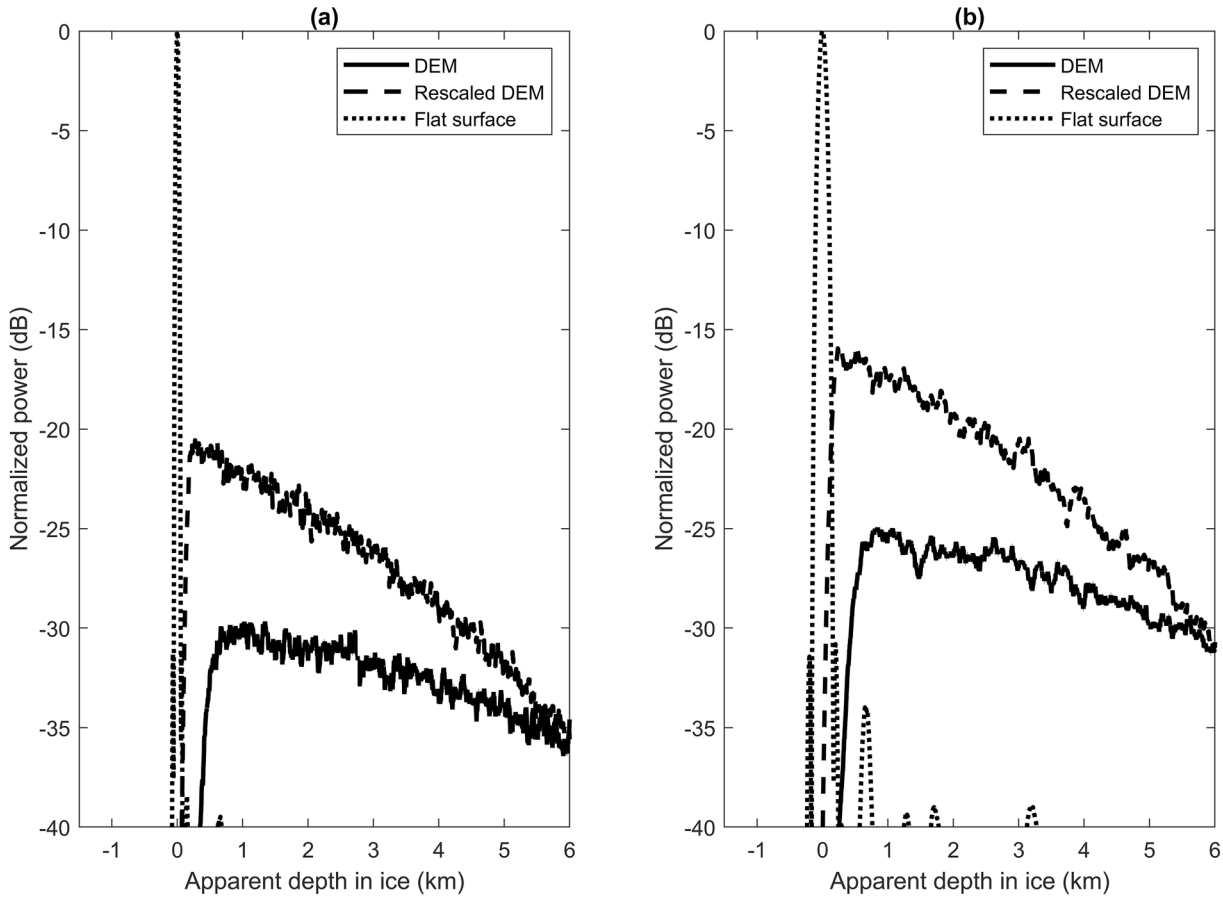

Figure 15. Median power of simulated radar echoes normalized to the power of the echo from a flat surface. (a) Echoes for a 3 MHz bandwidth pulse for the digital elevation models (DEMs) in Figures 13a and 13d. (b) Echoes for a 1 MHz bandwidth pulse for the DEMs in Figures 13a and 13d.

the echo power by 9.54 dB, that is, by a factor of 3 due to the elimination of two thirds of its Fourier spectrum and the in-phase summation of such spectral components in producing the coherent echo. Conversely, as the phase of spectral components in the diffuse echo spectrum is nearly random, suppressing two-thirds of its Fourier spectrum reduces the diffuse echo power by 4.5–5 dB, close to the square root of three. In practical terms, this means that reducing signal bandwidth is only partially effective in reducing clutter noise when the surface is so rough that scattering can be considered nearly incoherent.

Three-dimensional simulations of clutter effects on both surface and subsurface echo power have been presented by Heggy et al. (2017) and Gerekos et al. (2020). Clutter power decay rates obtained by Heggy et al. (2017) approach 50 dB/km highlighting the extent of the uncertainty in the modeling of radar scattering from the surface of Ganymede. The topography model in Heggy et al. (2017) was not based on any actual DEM but included fractures in brittle ice that affect propagation in the near subsurface and produce volume scattering appearing as clutter. Better terrain models with higher spatial sampling are a key factor in improving the quality and reliability of simulation results, but the resolution of existing images for stereo processing does not leave much room for possible improvement in this respect.

An alternative approach could be the one explored by Gerekos et al. (2021), who characterized the statistical properties of available topographic data sets for Ganymede and then considered higher resolution DEMs of Mars with similar values of statistical parameters to model the expected surface radar response. The greater potential source of inaccuracy, however, could be the structure of the surface at scales from meters to tens of meters, which are well below the possible resolution of any methodology used to produce DEMs of Ganymede before JUICE reaches the Jovian system. If topography at those scales is similar to what has been proposed for Europa by Hobley et al. (2018), then the coherent model of surface scattering employed in the present work will

be inadequate to study clutter, and predictions of its strength and decay rates will be based on models of incoherent scattering from random rough surfaces (e.g., Ogilvy, 1991). Furthermore, the unusual geometry of surface morphologies hypothesized by Hobley et al. (2018) would likely result in strong sensitivity of radar scattering to the angle between the azimuth direction of the spacecraft and the horizontal direction along which the vertical blades of ice are aligned. Despite these uncertainties, we still consider it worthwhile to extend the present study to other areas of Ganymede for which stereo-derived DEMs are available, improving the electromagnetic model of surface scattering for greater accuracy (see e.g., Gerekos et al., 2020; Heggy et al., 2017) and to compute simulated echoes that approach as closely as possible the expected altitude, ground track and spatial sampling rate expected for the real experiment.

Compared to simulations presented in Sbalchiero et al. (2022), the present work does not account for small-scale roughness superimposed on the discretized surface, nor employs a finite-difference time-domain (FDTD) technique to fully compute the scattered field, but it considers the full radar footprint in computing the resulting echo (limited only by the size of the DEM), and accounts for pulse-to-pulse phase variation of echoes from individual scatterers. For this reason, insofar as the facet method can be considered acceptable in simulating the radar echo, as discussed above, the simulator presented in this work can produce data that could be processed by testing different algorithms such as those presented in Sbalchiero et al. (2022).

The diffuse scattering in Figure 14, due to the random rough nature of the topography of Ganymede, is qualitatively different from simulations presented in Sbalchiero et al. (2022), who employed Martian and Venusian topographic analogs, but also a DEM of Ganymede complemented by subsurface features for FDTD computations. Although we suspect that the main reason for the difference is the value of statistical parameters such as r.m.s. height and r.m.s. slope in different DEMs, other factors such as DEM resolution and different computational methods may have an influence on results. We would certainly be interested in a comparison between results presented in both papers, but more important still would be a test of the effect of the processing scheme presented in Sbalchiero et al. (2022) in reducing or suppressing the diffuse echo in Figure 14.

More recently, Sbalchiero et al. (2023) published scattering simulation results that appear qualitatively similar to synthetic radargrams in Figure 14 (see Figure 5 in their work). Interestingly, they also applied a facet method and employed a synthetic DEM meant to represent grooved terrain on Ganymede. Although Sbalchiero et al. (2023) do not report explicitly the statistical properties of the synthetic DEM, their Table 2 can be used to reproduce it and estimate its statistics. Because of the way in which the synthetic topographic profile is defined, the distribution of slopes is markedly different from the one shown in Figure 13, but the median value is above 70°. Thus, insofar as median slopes of topography are of the order of several tens of degrees, surface echoes will diffuse with a slow decay rate with time, thus potentially masking subsurface echoes over a range of depths of several kilometers.

6. Discussion

In the case of the Nippur Sulcus region studied here, the combination of optical images, near infrared spectroscopic data and modeling, highlights the following points:

1. The grooves in the Epigeus ROI are pervasive, partially crosscutting or following the putative rim of an old palimpsest (*p1*) (Figure 3). The Epigeus palimpsest is confirmed to be the youngest feature of its size in the area since it is uncut by the grooves and its secondaries overlay the sulci (see also Jones et al. (2003)).
2. All terrain units show evidence of crystalline water ice (Figure 4, Figure 7). The *c2* crater showing up in the dark terrain has a composition similar to that of the young fresh crater within the palimpsest Epigeus, revealing that the dark material is not extended at great depths but rather limited to a superficial cortex. The presence of signatures of non-ice materials such as trapped/complexed CO_2 and organics in these "fresh" profiles reveals that these compounds may have an endogenous rather than exogenous origin. In turn, the grooves have a composition similar to that of small fresh craters, potentially indicative of material exchange between liquid interior and surface.
3. The vertical maximum extension of the connected groove network estimated in Nippur Sulcus, 125–135 km (Figure 11), potentially represents the thickness of the outer ice crust in that region. The distribution of the grooves suggests that their development may have occurred in two steps, with the largest grooves that could have cut the entire outer crust and the smaller grooves that could have developed at a later stage.

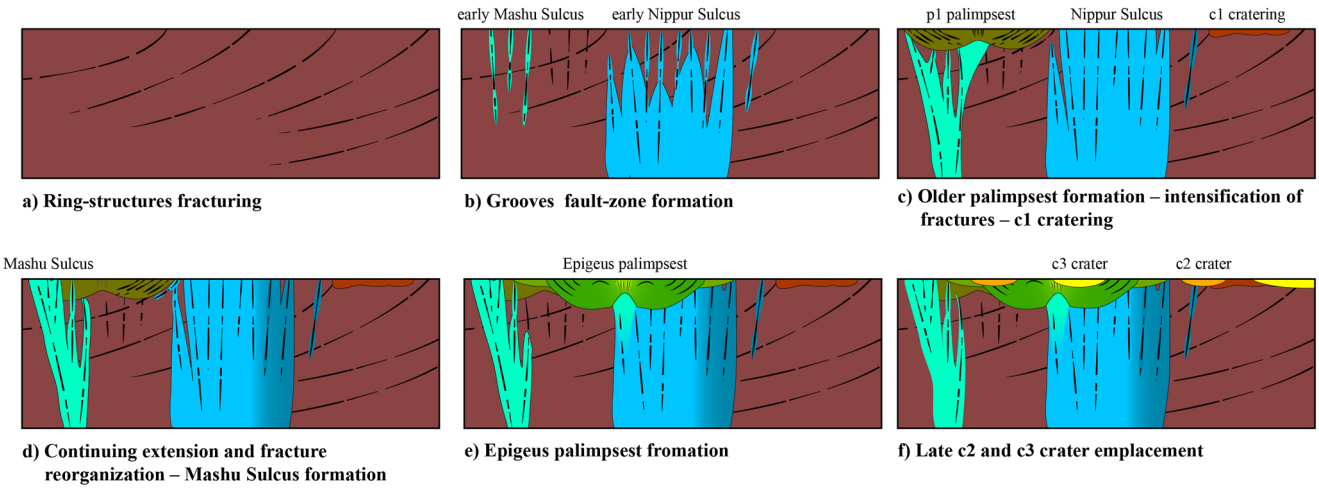

Figure 16. Temporal scheme (a–f) of the geological evolution of the Epigeus Region Of Interest (ROI) based on the chronostratigraphic interpretation of the region as inferred from the geological map in Figure 3. Features are not to scale and represent a hypothetical and simplified NE-SW cross-section of the ROI. Colors refer to the legend in Figure 3. Where fractures (dashed lines) are present, colors represent highly fractured fault zones.

By considering these findings together, the Epigeus ROI reveals an intriguing sequence of geological events that we schematically summarize in Figure 16.

The area is characterized by furrows encompassed in dark terrains (mapped as ring structures in Figure 3). These are the oldest known feature on Ganymede (Passey & Shoemaker, 1982) and are the surface expression of the concentric structures of a large multiring basin known as the Galileo-Marius furrow system (e.g., Schenk & McKinnon, 1987). Thus, an early scenario of the ROI is characterized by an intensely fractured crust with faults systematically dipping toward the old multiring basin center (Figure 16a). Further fracturing occurs at a later stage, when the main sulci started to form due to extensional tectonism (e.g., Pappalardo et al., 2004) and warmer ice possibly started to form along these fault zones due to local oblique friction (Figure 16b).

Overall, we observe that the sulci system gets older toward the east. While the eastern sulci facies are darker and more degraded, the western facies are brighter and fresher in morphology. Thus, melt resurfacing might have stopped earlier in the eastern groves (e.g., dark blue structures in Figure 16c). Some groove systems west of the Nippur sulcus seem to be interrupted by the presence of *p1* and run concentrically around it at the same time. This could be proof of a sin-tectonic *p1* impact, such that while the sulcus formation was developing from east to west, *p1* formed (Figure 16c). The major development of the western part of the sulcus must have happened after *p1*. In particular, the Mashu sulcus facies to the west is clearly the youngest branch of this sulci system since it neatly cuts *p1* (Figure 16d). There is not much evidence whether *c1* cratering happened at this stage or the previous stages, but the overall brightness and morphology of *c1* craters let us infer that they are older than the Mashu sulcus formation. Hence, the Epigeus crater palimpsest emplaced on top of this already complicated and densely fractured setting (Figure 16e). The Epigeus impact may also have favored the ascent of warm ice in its central fractured area. Palimpsest deposits are likely "fluid-rich continuous ejecta deposits resulting from an impact into an ice-rich target" (Jones et al., 2003). Hence, the Epigeus impact caused melting and mixing of the pre-impact crust, which was in turn already deeply fractured by the sulcus. The compounds brought up to the surface by the sulcus' fractures were thus likely spread out by the palimpsest impact. No groove crosscuts Epigeus, hinting at the fact that the tectonic activity in this area has stopped soon after the Epigeus impact. Finally, *c2* and *c3* craters formed just after this stage, disturbing and mixing only the superficial cortex (Figure 16f). Unfortunately, there is no unit that can help us constrain further stratigraphic detail occurring between *c2*- and *c3*-type cratering. In fact, these two crater classes are more distinct because of their albedo rather than because of their morphology. Hence, it is likely that these two classes are coeval at geological timescales and are only different because of the superficial cortex material that they excavated. For comparison, the *c3* crater on top of Epigeus centered at 180°E mixed the compounds of the ringed palimpsest facies, while the *c2* crater centered at 175°W caused the mixing of the ringed dark terrain materials (see Figure 4b), in both cases acting at very shallow depths.

Overall, given the numerous events that stressed the crust in this region, it is possible that large negatively buoyant lenses of melt remain seated below this area. Some open questions then arise: what is the surface composition of the grooves at a smaller local scale? Is the surface of Ganymede still connected to the ocean at the grooves, or was it only in the past, and if so, how long ago? Is it possible that the grooves also act as an escape route for underground liquid pockets located closer to the surface?

Future investigations of Ganymede's surface-subsurface interactions will require finer-scale multidisciplinary approaches to study ROIs such as this one.

7. Future Implications for JUICE

The *JUpiter Icy Moons Explorer* (JUICE) was selected in 2012 as the first large-class mission within the ESA *Cosmic Vision* program, with the primary goal of investigating the conditions of habitability and potential habitability existing in the system of Jupiter's icy Galilean moons. JUICE was designed to provide answers to the numerous questions left open by the previous close explorations of the Galilean satellites (Grasset et al., 2013). JUICE will be the first ever spacecraft to enter orbit around an icy satellite, Ganymede, ultimately allowing unprecedented analysis of its surface, interior and tenuous atmosphere. JUICE has a comprehensive suite of remote sensing instruments, covering the vast electromagnetic range from far ultraviolet to high frequency radio waves. The achievement of interdisciplinary objectives for a large-class space mission such as JUICE must necessarily start from well-developed scientific objectives that can be achieved in the various mission phases, considering the system resources and the performances of the individual payload instruments.

The *Jovis*, *Amorum ac Natorum Undique Scrutator* (JANUS) framing camera (Della Corte et al., 2019), sensitive in the spectral range 0.34–1.08 μm, is equipped with a panchromatic filter and 12 additional filters with both wide and narrow spectral bands, optimized to perform an in-depth study of satellites' surfaces and exospheres. At Ganymede, JANUS is expected to achieve global coverage with its panchromatic filter at a maximum ground sampling of 77 m/pixel and global color coverage (RGB filters) at 308 m/pixel. As many regions of interest as possible, among those identified in Stephan et al. (2021), will later be investigated at a ground sampling <10 m/pixel.

The *Moons And Jupiter Imaging Spectrometer* (MAJIS) (Piccioni et al., 2019) has both a wider spectral range (0.49–5.56 μm, sampled in about 1,000 channels) and a higher spectral sampling than similar instruments flown onboard past planetary spacecrafts (3.7 nm in the 0.49–2.36 μm range and 6.5 nm in the 2.27–5.56 μm range). Its main objective is to determine and map the surface composition of the satellites, with particular emphasis on non-water-ice materials such as hydrated minerals, volatile compounds, and organic compounds. MAJIS is committed to achieving nearly global coverage at a spatial resolution between 1 and 5 km/pixel (3 km/pixel on average), but several regions of interest will later be observed with a ground sampling <80 m/pixel.

Radio Echo Sounding is a geophysical technique used to detect the underground stratigraphy of a planetary body, such as the possible presence of liquid water under the polar caps of Mars with the MARSIS instrument onboard the ESA Mars Express spacecraft (Lauro et al., 2021; Orosei et al., 2018; Picardi et al., 2005). Similar to MARSIS, the *RIME* (Bruzzone & Croci, 2019) is a synthetic aperture radar onboard JUICE, operating at a central frequency of 9 MHz selected to allow exploration of the ice crusts up to a maximum depth of 9 km (Heggy et al., 2017). The main objective of this instrument is to characterize the geology and geophysics of the icy moons' subsurfaces, understand the formation of the geological features visible on the surface, the regional and global tectonics, look for traces of past and present activities, and identify the potential presence of underground liquid water. RIME will operate especially during the Ganymede low altitude circular orbit phase, focusing on the anti-Jovian side to limit the interference caused by Jupiter's radio emission and increase the SNR. JANUS, MAJIS, and RIME will be able to provide an unprecedented amount of data for Jupiter's icy moons system, with particular emphasis on Ganymede.

While MAJIS will shed new light on the nature of the non-ice material in terms of salts and organics, a combination of imaging spectroscopy data acquired by MAJIS and optical imagery of specific regions of interest returned by JANUS with a ground sampling 10 times higher is a natural evolution in data analysis and is aimed at the localization of homogeneous spectral units possibly connected to the subsurface. In the hypothesis that the surface composition is the result of a linear combination of spectral endmembers, one major complementarity between JANUS multispectral (color) data and hyperspectral images acquired by

MAJIS concerns the inference of the composition at spatial scales that will be inaccessible to MAJIS. In other words, by degrading the spatial resolution of the JANUS data to that of MAJIS, a given slope of the spectral continuum or color obtained through a JANUS RGB composite image should ideally correspond to the same spectral slope or color as measured by MAJIS in the spectral range 0.5–1.0 μm where the sensitivity ranges of these two instruments overlap, within the limits imposed by the bandwidth of the filters and by the instrumental noise (once in orbit around Ganymede, in certain cases it will be possible to simultaneously observe the same region at the highest spatial resolution both with JANUS and MAJIS, thus ensuring homogeneous solar illumination conditions). In these cases, JANUS multispectral data could ideally be used to infer and map the surface composition of local-scale geological features at ground sampling (<70 m/pixel) inaccessible to the spectrometers.

The radar is a direct and powerful technique to investigate the upper few kilometers of the conductive ice shell of Ganymede, including potential underground liquid pockets showing a strong dielectric contrast with respect to the surrounding icy crust. However, one practical issue that RIME will have to face is the diffusion of the surface echo from directions other than the nadir, called "clutter," which must be appropriately treated in the data analysis to effectively achieve the scientific objective of measuring the underground stratigraphy and revealing any subsurface liquid reservoirs. Ganymede is generally rougher than Europa. In Nippur Sulcus, for which no stereo-derived DTMs are available, our analysis shows that with a synthetic but reasonable topography derived from a single high-resolution optical image, the clutter-induced noise is substantial. This requires a good knowledge of the topography itself, to be derived in the future with direct JUICE measurements, in order to correctly extract the signal coming from any real subsurface structures.

The example investigation proposed here falls within the top-level goal that the JUICE mission aims to achieve, namely assessing the potential habitability of Ganymede. The JUICE mission, launched on 14 April 2023, will have the possibility of obtaining much better data than those available so far regarding the geology and surface composition of Ganymede, and completely new data regarding the subsurface. The combination of multi- and hyperspectral data obtained from JANUS and MAJIS, respectively, with the radargrams obtained from RIME will be fundamental to allow a direct correlation between the surface and subsurface. In turn, this correlation is key to revealing those regions where the exchange of material between the surface and the subsurface has been more intense and frequent in Ganymede's recent past, ultimately providing a 3D view of the physical processes that shaped its surface and are representative of peculiar phases of its evolution.

The correlation between wide-ranging scientific objectives such as geology, surface composition and geophysics, usually addressed by a single instrument or by a single category of instruments, is crucial for evaluating the potential habitability of icy satellites. The main strength deriving from the joint use of diverse remote sensing data is the characterization of specific regions of interest observed by both the camera and the spectrometer(s) at an unprecedented spatial resolution, complemented by a first time ever subsurface investigation which could ultimately provide a 3D view revealing connections between the surface and the subsurface.

Preparing as of now case studies such as that of Nippur Sulcus has the advantage of emphasizing the potential of a future combination of data obtained from the JANUS, MAJIS, and RIME instruments onboard JUICE on specific regions of interest observed at high spatial resolution and with adequate SNR. Such a multisensor data analysis could benefit and broaden even more by the addition of further results from other JUICE instruments, such as the Ultraviolet Spectrograph, which will acquire spectra of Ganymede in the far ultraviolet range 50–204 nm at spatial scales ranging from several km/pixel to <1 km/pixel, the GALA laser altimeter, which will obtain global-scale topography of Ganymede (to be compared with much smaller optical stereo coverage) (Enya et al., 2022), the 3GM radio science experiment, which could provide a connection with the mass distribution existing at depths substantially greater than those probed by RIME (De Marchi et al., 2021), and the plasma and particles package PEP, whose mass spectrometer NIM sensor (Föhn et al., 2021) could reveal sources and sinks of neutral atoms connecting Ganymede's tenuous atmosphere to its surface.

In the future, our analysis could be expanded to other regions of interest on Ganymede for which adequate coverage is available.

Data Availability Statement

Galileo SSI and NIMS data sets of Ganymede are archived in NASA's Planetary Data System (PDS) and can be found in Thaller (2000) and Carlson (1998), respectively. The mapping of optical and near infrared spectroscopic data was performed using the commercial software ArcGIS (https://www.arcgis.com/home/index.html). The spectral analysis, the self-similar clustering analysis and the derivation of synthetic topography for the Nippur Sulcus region were performed using homemade software developed in the commercial IDL language (https://www.l3harrisgeospatial.com/Software-Technology/IDL). The analysis of clutter-induced radar noise was performed using homemade software developed in the commercial Matlab language (https://www.mathworks.com/products/matlab.html). Data sets for this research are available in Tosi et al. (2022).

Acknowledgments
This research is the result of the Mainstream INAF project: "*Ganimede dal 2D al 3D*: *Un approccio multidisciplinare in preparazione a JUICE*," selected by the Scientific Directorate of Italy's National Institute for Astrophysics (INAF) on 25 March 2019 and funded with 34,000 euros (INAF Grant 1.05.01.86.27). This research has made use of the USGS Integrated Software for Imagers and Spectrometers (ISIS) and NASA's Astrophysics Data System (NASA-ADS).

References

Ackermann, R. V., Schlische, R. W., & Withjack, M. O. (2001). The geometric and statistical evolution of normal fault systems: An experimental study of the effects of mechanical layer thickness on scaling laws. *Journal of Structural Geology*, *23*(11), 1803–1819. https://doi.org/10.1016/S0191-8141(01)00028-1

Becker, T., Archinal, B., Colvin, T., Davies, M., Gitlin, A., Kirk, R. L., et al. (2001). Final digital global maps of Ganymede, Europa, and Callisto. In *Lunar and planetary science conference* (p. 2009).

Belton, M. J. S., Klaasen, K. P., Clary, M. C., Anderson, J. L., Anger, C. D., Carr, M. H., et al. (1992). The Galileo solid-state imaging experiment. *Space Science Reviews*, *60*(1–4), 413–455. https://doi.org/10.1007/BF00216864

Benedicto, A., Schultz, R. A., & Soliva, R. (2003). Layer thickness and the shape of faults. *Geophysical Research Letters*, *30*(20), 2076. https://doi.org/10.1029/2003GL018237

Berquin, Y., Kofman, W., Herique, A., Alberti, G., & Beck, P. (2013). A study on Ganymede's surface topography: Perspectives for radar sounding. *Planetary and Space Science*, *77*, 40–44. https://doi.org/10.1016/j.pss.2012.07.004

Bianchi, R., Casacchia, R., Lanciano, P., Pozio, S., & Strom, R. G. (1986). Tectonic framework of grooved terrain on Ganymede. *Icarus*, *67*(2), 237–250. https://doi.org/10.1016/0019-1035(86)90106-5

Black, G. J., Campbell, D. B., & Nicholson, P. D. (2001). Icy Galilean satellites: Modeling radar reflectivities as a coherent backscatter effect. *Icarus*, *151*(2), 167–180. https://doi.org/10.1006/icar.2001.6616

Black, G. J., Campbell, D. B., & Ostro, S. J. (2001). Icy Galilean satellites: 70 cm radar results from Arecibo. *Icarus*, *151*(2), 160–166. https://doi.org/10.1006/icar.2001.6615

Bonnet, E., Bour, O., Odling, N. E., Davy, P., Main, I., Cowie, P., & Berkowitz, B. (2001). Scaling of fracture systems in geological media. *Reviews of Geophysics*, *39*(3), 347–383. https://doi.org/10.1029/1999RG000074

Bour, O., & Davy, P. (1999). Clustering and size distributions of fault patterns: Theory and measurements. *Geophysical Research Letters*, *16*(13), 2001–2004. https://doi.org/10.1029/1999GL900419

Bour, O., Davy, P., Darcel, C., & Odling, N. (2002). A statistical scaling model for fracture network geometry, with validation on a multiscale mapping of a joint network (Hornelen Basin, Norway). *Journal of Geophysical Research*, *107*(B6), ETG4-1–ETG4-12. https://doi.org/10.1029/2001JB000176

Bruzzone, L., Alberti, G., Catallo, C., Ferro, A., Kofman, W., & Orosei, R. (2011). Subsurface radar sounding of the Jovian moon Ganymede. *Proceedings of the IEEE*, *99*(5), 837–857. https://doi.org/10.1109/JPROC.2011.2108990

Bruzzone, L., & Croci, R. (2019). Radar for icy moon exploration (RIME). In *Proceeding of the 2019 IEEE 5th international workshop on metrology for AeroSpace (MetroAeroSpace)*. https://doi.org/10.1109/MetroAeroSpace.2019.8869624

Cameron, M. E., Smith-Konter, B. R., Burkhard, L., Collins, G. C., Seifert, F., & Pappalardo, R. T. (2018). Morphological mapping of Ganymede: Investigating the role of strike-slip tectonics in the evolution of terrain types. *Icarus*, *315*, 92–114. https://doi.org/10.1016/j.icarus.2018.06.024

Carlson, R. W. (1998). Galileo NIMS spectral image cubes: Jupiter operations [Dataset]. NASA Planetary Data System. https://doi.org/10.17189/1520371

Carlson, R. W., Weissman, P. R., Smythe, W. D., & Mahoney, J. C., & the NIMS Science and Engineering Team. (1992). Near-infrared mapping spectrometer experiment on Galileo. *Space Science Reviews*, *60*(1–4), 457–502. https://doi.org/10.1007/978-94-011-2512-3_18

Chicarro, A. (2002). Mars Express mission and astrobiology. *Solar System Research*, *36*(6), 487–491. https://doi.org/10.1023/A:1022153103030

Clark, R. N. (1999). Spectroscopy of rocks and minerals, and principles of spectroscopy. In A. N. Rencz (Ed.), *Remote sensing for the Earth sciences, manual of remote sensing* (Vol. 3, pp. 3–58). John Wiley and Sons.

Collins, G. C., Patterson, G. W., Head, J. W., Prockter, L., Pappalardo, R. T., Lucchitta, B. K., & Kay, J. P. (2013). *Global geologic map of Ganymede* (p. 3237). US Department of the Interior, US Geological Survey. https://doi.org/10.3133/sim3237

Cowie, P. A., Malinverno, A., Ryan, W. B. F., & Edwards, M. H. (1994). Quantitative fault studies on the east Pacific rise: A comparison of sonar imaging techniques. *Journal of Geophysical Research*, *99*(B8), 15205–15218. https://doi.org/10.1029/94JB00041

Della Corte, V., Noci, G., Turella, A., Paolinetti, R., Zusi, M., Michaelis, H., et al. (2019). Scientific objectives of JANUS Instrument onboard JUICE mission and key technical solutions for its Optical Head. In *Proceeding of the 2019 IEEE 5th international workshop on metrology for AeroSpace (MetroAeroSpace)*. https://doi.org/10.1109/MetroAeroSpace.2019.8869584

De Marchi, F., Di Achille, G., Mitri, G., Cappuccio, P., Di Stefano, I., Di Benedetto, M., & Luciano, I. (2021). Observability of Ganymede's gravity anomalies related to surface features by the 3GM experiment onboard ESA's JUpiter ICy moons Explorer (JUICE) mission. *Icarus*, *354*, 114003. https://doi.org/10.1016/j.icarus.2020.114003

Enya, K., Kobayashi, M., Kimura, J., Araki, H., Namiki, N., Noda, H., et al. (2022). The Ganymede laser altimeter (GALA) for the Jupiter icy moons explorer (JUICE): Mission, science, and instrumentation of its receiver modules. *Advances in Space Research*, *69*(5), 2283–2304. https://doi.org/10.1016/j.asr.2021.11.036

Fan, M., Lyu, P., Su, Y., Du, K., Zhang, Q., Zhang, Z., et al. (2021). The Mars orbiter subsurface investigation radar (MOSIR) on China's Tianwen-1 mission. *Space Science Reviews*, *217*(1), 8. https://doi.org/10.1007/s11214-020-00786-4

Filacchione, G., Capaccioni, F., Ciarniello, M., Clark, R. N., Cuzzi, J. N., Nicholson, P. D., et al. (2012). Saturn's icy satellites and rings investigated by Cassini–VIMS: III – Radial compositional variability. *Icarus*, *220*(2), 1064–1096. https://doi.org/10.1016/j.icarus.2012.06.040

Föhn, M., Galli, A., Vorburger, A., Tulej, M., Lasi, D., Riedo, A., et al. (2021). Description of the mass spectrometer for the Jupiter icy moons explorer. In *IEEE aerospace conference* (pp. 1–14). https://doi.org/10.1109/AERO50100.2021.9438344

Fulvio, D., Popa, C., Mennella, V., Tosi, F., De Angelis, S., Ciarniello, M., et al. (2023). Studying the temperature dependence of NIR reflectance spectra of selected hydrated salts dissolved in water: The case of natron, mirabilite and epsomite as representative for icy-world surfaces. *Icarus*, *394*, 115444. https://doi.org/10.1016/j.icarus.2023.115444

Gerekos, C., Bruzzone, L., & Imai, M. (2020). A Coherent method for simulating active and passive radar sounding of the Jovian icy moons. *IEEE Transactions on Geoscience and Remote Sensing*, *58*(4), 2250–2265. https://doi.org/10.1109/TGRS.2019.2945079

Gerekos, C., Grima, C., Steinbrügge, G., Thakur, S., Scanlan, K. M., Young, D. A., et al. (2021). Martian roughness analogues of European terrains for radar sounder investigations. *Icarus*, *358*, 114197. https://doi.org/10.1016/j.icarus.2020.114197

Grasset, O., Dougherty, M. K., Coustenis, A., Bunce, E. J., Erd, C., Titov, D., et al. (2013). JUpiter ICy moons Explorer (JUICE): An ESA mission to orbit Ganymede and to characterise the Jupiter system. *Planetary and Space Science*, *78*, 1–21. https://doi.org/10.1016/j.pss.2012.12.002

Greeley, R., Pappalardo, R. T., Prockter, L. M., Hendrix, A. R., & Lock, R. E. (2009). Europa. In R. T. Pappalardo, W. B. McKinnon, & K. Khurana (Eds.), *Future exploration of Europa* (pp. 655–696). University of Arizona Press.

Gudmundsson, A. (2012). *Rock fractures in geological processes* (p. 594). Cambridge University Press. https://doi.org/10.1017/CBO9780511975684

Gudmundsson, A., De Guidi, G., & Scudero, S. (2013). Length-displacement scaling and fault growth. *Tectonophysics*, *608*, 1298–1309. https://doi.org/10.1016/j.tecto.2013.06.012

Gudmundsson, A., Simmenes, T. H., Larsen, B., & Philipp, S. J. (2010). Effects of internal structure and local stresses on fracture propagation, deflection, and arrest in fault zones. *Journal of Structural Geology*, *32*(11), 1643–1655. https://doi.org/10.1016/j.jsg.2009.08.013

Guest, J. E., Bianchi, R., & Greeley, R. (1988). *Geologic map of the Uruk sulcus quadrangle of Ganymede*. US Geological Survey. IMAP 1934. https://doi.org/10.3133/i1934

Harris, F. J. (1978). On the use of windows for harmonic analysis with the discrete Fourier transform. *Proceedings of the IEEE*, *66*(1), 51–83. https://doi.org/10.1109/PROC.1978.10837

Head, J., Pappalardo, R., Collins, G., Belton, M. J. S., Giese, B., Wagner, R., et al. (2002). Evidence for Europa-like tectonic resurfacing styles on Ganymede. *Geophysical Research Letters*, *29*(24), 2151–2154. https://doi.org/10.1029/2002GL015961

Heggy, E., Scabbia, G., Bruzzone, L., & Pappalardo, R. T. (2017). Radar probing of Jovian icy moons: Understanding subsurface water and structure detectability in the JUICE and Europa missions. *Icarus*, *285*, 237–251. https://doi.org/10.1016/j.icarus.2016.11.039

Hobley, D. E. J., Moore, J. M., Howard, A. D., & Umurhan, O. M. (2018). Formation of metre-scale bladed roughness on Europa's surface by ablation of ice. *Nature Geoscience*, *11*(12), 901–904. https://doi.org/10.1038/s41561-018-0235-0

Ilyushin, Y. A., Orosei, R., Witasse, O., & Sánchez-Cano, B. (2017). CLUSIM: A synthetic aperture radar clutter simulator for planetary exploration. *Radio Science*, *52*(9), 1200–1213. https://doi.org/10.1002/2017RS006265

Johnson, T. V., Yeates, C. M., & Young, R. (1992). Space science reviews volume on Galileo Mission overview. *Space Science Reviews*, *60*(1–4), 3–21. https://doi.org/10.1007/BF00216848

Jones, K. B., Head, J. W., Pappalardo, R. T., & Moore, J. M. (2003). Morphology and origin of palimpsests on Ganymede based on Galileo observations. *Icarus*, *164*(1), 197–212. https://doi.org/10.1016/S0019-1035(03)00128-3

Kersten, E., Zubarev, A. E., Roatsch, T., & Matz, K.-D. (2021). Controlled global Ganymede mosaic from Voyager and Galileo images. *Planetary and Space Science*, *206*, 105310. https://doi.org/10.1016/j.pss.2021.105310

King, O., & Fletcher, L. N. (2022). Global Modeling of Ganymede's surface composition: Near-IR mapping from VLT/SPHERE. *Journal of Geophysical Research: Planets*, *127*(12), e2022JE007323. https://doi.org/10.1029/2022JE007323

Kivelson, M. G., Khurana, K. K., & Volwerk, M. (2002). The permanent and inductive magnetic moments of Ganymede. *Icarus*, *157*(2), 507–522. https://doi.org/10.1006/icar.2002.6834

Lauro, S. E., Pettinelli, E., Caprarelli, G., Guallini, L., Rossi, A. P., Mattei, E., et al. (2021). Multiple subglacial water bodies below the south pole of Mars unveiled by new MARSIS data. *Nature Astronomy*, *5*(1), 63–70. https://doi.org/10.1038/s41550-020-1200-6

Leonard, E. J., Yin, A., & Pappalardo, R. T. (2020). Ridged plains on Europa reveal a compressive past. *Icarus*, *343*, 113709. https://doi.org/10.1016/j.icarus.2020.113709

Lesage, E., Schmidt, F., Andrieu, F., & Massol, H. (2021). Constraints on effusive cryovolcanic eruptions on Europa using topography from Galileo images. *Icarus*, *361*, 114373. https://doi.org/10.1016/j.icarus.2021.114373

Ligier, N., Paranicas, C., Carter, J., Poulet, F., Calvin, W. M., Nordheim, T. A., et al. (2019). Surface composition and properties of Ganymede: Updates from ground-based observations with the near-infrared imaging spectrometer SINFONI/VLT/ESO. *Icarus*, *333*, 496–515. https://doi.org/10.1016/j.icarus.2019.06.013

Lucchetti, A., Dalle Ore, C., Pajola, M., Pozzobon, R., Rossi, C., Galluzzi, V., et al. (2023). Geological, compositional and crystallinity analysis of the Melkart impact crater, Ganymede. *Icarus*, *401*, 115613. https://doi.org/10.1016/j.icarus.2023.115613

Lucchetti, A., Pozzobon, R., Mazzarini, F., Cremonese, G., & Massironi, M. (2017). Brittle ice shell thickness of Enceladus from fracture distribution analysis. *Icarus*, *297*, 252–264. https://doi.org/10.1016/j.icarus.2017.07.009

Lucchetti, A., Rossi, C., Mazzarini, F., Pajola, M., Pozzobon, R., Massironi, M., & Cremonese, G. (2021). Equatorial grooves distribution on Ganymede: Length and self-similar clustering analysis. *Planetary and Space Science*, *195*, 105140. https://doi.org/10.1016/j.pss.2020.105140

Lucchitta, B. K. (1980). Grooved terrain on Ganymede. *Icarus*, *44*(2), 481–501. https://doi.org/10.1016/0019-1035(80)90039-1

Mazzarini, F. (2004). Volcanic vent self-similar clustering and crustal thickness in the northern Main Ethiopian Rift. *Geophysical Research Letters*, *31*(4), L04604. https://doi.org/10.1029/2003GL018574

Mazzarini, F., & Isola, I. (2010). Monogenetic vent self-similar clustering in extending continental crust: Examples from the East African Rift System. *Geosphere*, *6*(5), 567–582. https://doi.org/10.1130/GES00569.1

Mazzarini, F., Keir, D., & Isola, I. (2013). Spatial relationship between earthquakes and volcanic vents in the central-northern Main Ethiopian Rift. *Journal of Volcanology and Geothermal Research*, *262*, 123–133. https://doi.org/10.1016/j.jvolgeores.2013.05.007

McCord, T. B., Carlson, R., Smythe, W., Hansen, G., Clark, R., Hibbitts, C., et al. (1997). Organics and other molecules in the surfaces of Callisto and Ganymede. *Science*, *278*(5336), 271–275. https://doi.org/10.1126/science.278.5336.271

Mouginot, J., Kofman, W., Safaeinili, A., Grima, C., Herique, A., & Plaut, J. J. (2009). MARSIS surface reflectivity of the south residual cap of Mars. *Icarus*, *201*(2), 454–459. https://doi.org/10.1016/j.icarus.2009.01.009

Mouginot, J., Pommerol, A., Beck, P., Kofman, W., & Clifford, S. M. (2012). Dielectric map of the Martian northern hemisphere and the nature of plain filling materials. *Geophysical Research Letters*, *39*(2), L02202. https://doi.org/10.1029/2011GL050286

Mouginot, J., Pommerol, A., Kofman, W., Beck, P., Schmitt, B., Herique, A., et al. (2010). The 3–5 MHz global reflectivity map of Mars by MARSIS/Mars Express: Implications for the current inventory of subsurface H_2O. *Icarus*, *210*(2), 612–625. https://doi.org/10.1016/j.icarus.2010.07.003

Murchie, S. L., & Head, J. W., III. (1989). *Geologic map of the Philus sulcus quadrangle of Ganymede*. US Geological Survey. IMAP 1966. https://doi.org/10.3133/i1966

Nouvel, J.-F., Herique, A., Kofman, W., & Safaeinili, A. (2004). Radar signal simulation: Surface modeling with the facet method. *Radio Science*, *39*(1), RS1013. https://doi.org/10.1029/2003RS002903

Ogilvy, J. A. (1991). *Theory of wave scattering from random rough surfaces*. Adam Hilger.

Ono, T., Kumamoto, A., Nakagawa, H., Yamaguchi, Y., Oshigami, S., Yamaji, A., et al. (2009). Lunar Radar Sounder observations of subsurface layers under the nearside Maria of the Moon. *Science*, *323*(5916), 909–912. https://doi.org/10.1126/science.1165988

Orosei, R., Lauro, S. E., Pettinelli, E., Cicchetti, A., Coradini, M., Cosciotti, B., et al. (2018). Radar evidence of subglacial liquid water on Mars. *Science*, *361*(6401), 490–493. https://doi.org/10.1126/science.aar7268

Orosei, R., Rossi, A. P., Cantini, F., Caprarelli, G., Carter, L. M., Papiano, I., et al. (2017). Radar sounding of Lucus Planum, Mars, by MARSIS. *Journal of Geophysical Research: Planets*, *122*(7), 1405–1418. https://doi.org/10.1002/2016JE005232

Pappalardo, R. T., Collins, G. C., Head, J. W., III, Helfenstein, P., McCord, T. B., Moore, J. M., et al. (2004). Geology of Ganymede. In F. Bagenal, T. E. Dowling, W. B. McKinnon (Eds.),, & Cambridge Planetary Science (Eds.), *Jupiter. The planet, satellites and magnetosphere* (Vol. 1, pp. 363–396). Cambridge University Press.

Pappalardo, R. T., & Greeley, R. (1995). A review of the origins of subparallel ridges and troughs: Generalized morphological predictions from terrestrial models. *Journal of Geophysical Research*, *100*(E9), 18985–19007. https://doi.org/10.1029/94JE02638

Pappalardo, R. T., Head, J. W., Collins, G. C., Kirk, R. L., Neukum, G., Oberst, J., et al. (1998). Grooved terrain on Ganymede: First results from Galileo high-resolution imaging. *Icarus*, *135*(1), 276–302. https://doi.org/10.1006/icar.1998.5966

Passey, Q. R., & Shoemaker, E. M. (1982). Craters and basins on Ganymede and Callisto-Morphological indicators of crustal evolution. In *Satellites of Jupiter (A83-16226 04-91* (pp. 379–434). University of Arizona Press Satellites.

Patterson, G. W., Collins, G. C., Head, J. W., Pappalardo, R. T., Prockter, L. M., Lucchitta, B. K., & Kay, J. P. (2010). Global geological mapping of Ganymede. *Icarus*, *207*(2), 845–867. https://doi.org/10.1016/j.icarus.2009.11.035

Phillips, R. J., Adams, G. F., Brown, W. E., Jr., Eggleton, R. E., Jackson, P., Jordan, R., et al. (1973). Apollo lunar sounder experiment. NASA Apollo 17 Preliminary Science Report, Document SP-330. Retrieved from https://www.hq.nasa.gov/alsj/a17/as17psr.pdf

Picardi, G., Biccari, D., Seu, R., Marinangeli, L., Johnson, T. K., Jordan, R. L., et al. (2004). Performance and surface scattering models for the Mars advanced radar for subsurface and ionosphere sounding (MARSIS). *Planetary and Space Science*, *52*(1–3), 149–156. https://doi.org/10.1016/j.pss.2003.08.020

Picardi, G., Plaut, J. J., Biccari, D., Bombaci, O., Calabrese, D., Cartacci, M., et al. (2005). Radar soundings of the subsurface of Mars. *Science*, *310*(5756), 1925–1928. https://doi.org/10.1126/science.1122165

Piccioni, G., Tommasi, L., Langevin, Y., Filacchione, G., Tosi, F., Grassi, D., et al. (2019). Scientific goals and technical challenges of the MAJIS imaging spectrometer for the JUICE mission. In *Proceedings of the 2019 IEEE 5th international workshop on metrology for AeroSpace (MetroAeroSpace)*. https://doi.org/10.1109/MetroAeroSpace.2019.8869566

Rossi, C., Cianfarra, P., & Salvini, F. (2020). Structural geology of Ganymede regional groove systems (60°N–60°S). *Journal of Maps*, *16*(2), 6–16. https://doi.org/10.1080/17445647.2019.1685605

Russo, F., Cutigni, M., Orosei, R., Taddei, C., Seu, R., Biccari, D., et al. (2008). An incoherent simulator for the SHARAD experiment. In *2008 IEEE radar conference*. https://doi.org/10.1109/RADAR.2008.4720761

Saur, J., Duling, S., Roth, L., Jia, X., Strobel, D. F., Feldman, P. D., et al. (2015). The search for a subsurface ocean in Ganymede with Hubble Space Telescope observations of its auroral ovals. *Journal of Geophysical Research: Space Physics*, *120*(3), 1715–1737. https://doi.org/10.1002/2014JA020778

Sbalchiero, E., Thakur, S., & Bruzzone, L. (2022). A Range-Doppler method for focusing radar sounder data generated by coherent electromagnetic simulators. *IEEE Transactions on Geoscience and Remote Sensing*, *60*, 1–19. https://doi.org/10.1109/TGRS.2022.3201047

Sbalchiero, E., Thakur, S., Cortellazzi, M., & Bruzzone, L. (2023). Subsurface signatures of bright terrain formation models on Ganymede by 3D radar sounder simulations. *Icarus*, *394*, 115351. https://doi.org/10.1016/j.icarus.2022.115351

Schenk, P. M. (2002). Thickness constraints on the icy shells of the Galilean satellites from a comparison of crater shapes. *Nature*, *417*(6887), 419–421. https://doi.org/10.1038/417419a

Schenk, P. M. (2009). Slope characteristics of Europa: Constraints for landers and radar sounding. *Geophysical Research Letters*, *36*(15), L15204. https://doi.org/10.1029/2009GL039062

Schenk, P. M., & McKinnon, W. B. (1987). Ring geometry on Ganymede and Callisto. *Icarus*, *72*(1), 209–234. https://doi.org/10.1016/0019-1035(87)90126-6

Schultz, R. A., Soliva, R., Okubo, C. H., & Mège, D. (2010). Fault populations. In T. R. Watters & R. A. Schultz (Eds.), *Planetary tectonics* (pp. 457–510). Cambridge University Press. https://doi.org/10.1017/CBO9780511691645.011

Seu, R., Phillips, R. J., Biccari, D., Orosei, R., Masdea, A., Picardi, G., et al. (2007). SHARAD sounding radar on the Mars Reconnaissance Orbiter. *Journal of Geophysical Research*, *112*(E5), E05S05. https://doi.org/10.1029/2006JE002745

Skinner, J. A., Jr., Huff, A. E., Fortezzo, C. M., Gaither, T. A., Hare, T. M., & Hunter, M. A. (2018). Planetary geologic mapping protocol–2018. Retrieved from https://astropedia.astrogeology.usgs.gov/download/Docs/Mappers/PGM_Protocol_March_2018.pdf

Smith, D. E., Zuber, M. T., Frey, H. V., Garvin, J. B., Head, J. W., Muhleman, D. O., et al. (2001). Mars Orbiter Laser Altimeter: Experiment summary after the first year of global mapping of Mars. *Journal of Geophysical Research*, *106*(E10), 23689–23722. https://doi.org/10.1029/2000JE001364

Soliva, R., & Schultz, R. A. (2008). Distributed and localized faulting in extensional settings: Insight from the North Ethiopian Rift–Afar transition area. *Tectonics*, *27*(2), TC2003. https://doi.org/10.1029/2007TC002148

Spagnuolo, M. G., Grings, F., Perna, P., Franco, M., Karszenbaum, H., & Ramos, V. A. (2011). Multilayer simulations for accurate geological interpretations of SHARAD radargrams. *Planetary and Space Science*, *59*(11–12), 1222–1230. https://doi.org/10.1016/j.pss.2010.10.013

Steinbrügge, G., Voigt, J. R. C., Schroeder, D. M., Stark, A., Haynes, M. S., Scanlan, K. M., et al. (2020). The surface roughness of Europa derived from Galileo stereo images. *Icarus*, *343*, 113669. https://doi.org/10.1016/j.icarus.2020.113669

Stephan, K., Hibbitts, C. A., & Jaumann, R. (2020). H_2O-ice particle size variations across Ganymede's and Callisto's surface. *Icarus*, *337*, 113440. https://doi.org/10.1016/j.icarus.2019.113440

Stephan, K., Roatsch, T., Tosi, F., Matz, K.-D., Kersten, E., Wagner, R., et al. (2021). Regions of interest on Ganymede's and Callisto's surfaces as potential targets for ESA's JUICE mission. *Planetary and Space Science*, *208*, 105324. https://doi.org/10.1016/j.pss.2021.105324

Stratton, J. A. (1941). Electromagnetic theory. In *International series in physics*. McGraw-Hill Book Company, Inc.

Thaller, T. F. (2000). Galileo orbital operations solid state imaging raw EDR V1.0 [Dataset]. NASA Planetary Data System. https://doi.org/10.17189/1520425

Tosi, F., Galluzzi, V., Lucchetti, A., Orosei, R., Filacchione, G., Zambon, F., et al. (2022). Multidisciplinary analysis of the Nippur sulcus region on Ganymede [Dataset]. Zenodo. https://doi.org/10.5281/zenodo.7341462

Underwood, J. R., Jr., Casacchia, R., Woronow, A., & Teeling, M. J. (1997). *Geologic map of the Galileo Regio quadrangle (Jg-3) of Ganymede*. US Geological Survey. IMAP 2534. https://doi.org/10.3133/i2534

Zubarev, A., Nadezhdina, I., Brusnikin, E., Giese, B., & Oberst, J. (2017). A search for Ganymede stereo images and 3D mapping opportunities. *Planetary and Space Science*, *146*, 40–54. https://doi.org/10.1016/j.pss.2017.07.021

Erratum

In the originally published version of this article, the unit of measure "μm" was incorrectly omitted after the value 2.36 in the first sentence of the third paragraph of Section 7. The sentence should read: "3.7 nm in the 0.49–2.36 μm range." In addition, In the caption for figure 4, "(g) 2.02 μm" should be changed to "G: 2.02 μm," and "(b) 1.21 μm" should be changed to "B: 1.21 μm." In the caption for figure 6, "(g) 2-μm" should be changed to "G: 2-μm," and "(b) IR ratio" should be changed to "B: IR ratio." The errors have been corrected, and this may be considered the authoritative version of record.